

# Changes in Stratospheric Climate and Age-of-Air in Recent GEOS Systems since MERRA-2

Clara Orbe<sup>1,2</sup>, Lawrence L. Takacs<sup>3,4</sup>, Amal El Akkroui<sup>3</sup>,  
Krzysztof Wargan<sup>3,4</sup>, Andrea Molod<sup>3</sup>, Steven Pawson<sup>3</sup>

<sup>1</sup>NASA Goddard Institute for Space Studies, New York, NY

<sup>2</sup>Department of Applied Physics and Applied Mathematics, Columbia University, New York, NY

<sup>3</sup>Global Modeling and Assimilation Office, NASA Goddard Space Flight Center, Greenbelt, MD

<sup>4</sup>Science Systems and Applications, Inc., Lanham, MD, USA

## Key Points:

- The stratospheric mean age-of-air simulated in GEOS is sensitive to the remapping scheme used within the finite-volume dynamical core.
- This sensitivity in the age-of-air is large ( $\sim 30\%$ ) and imprints on the simulated distributions of several long-lived trace gases (e.g.,  $N_2O$ ,  $CH_4$ ).
- The age-of-air sensitivities primarily reflect changes in resolved wave convergence over the NH extratropical stratosphere.

---

Corresponding author: Clara Orbe, [clara.orbe@nasa.gov](mailto:clara.orbe@nasa.gov)

## 16 Abstract

17 Accurately modeling the large-scale transport of trace gases and aerosols is critical for interpreting past (and projecting future) changes in atmospheric composition. 18 Simulations of the stratospheric mean age-of-air continue to show persistent biases in chemistry climate models, although the drivers of these biases are not well understood. Here 19 we identify one driver of simulated stratospheric transport differences among various NASA 20 Global Earth Observing System (GEOS) candidate model versions under consideration 21 for the upcoming GEOS Retrospective analysis for the 21<sup>st</sup> Century (GEOS-R21C). In 22 particular, we show that the simulated age-of-air values are sensitive to the so-called “remap- 23 ping” algorithm used within the finite-volume dynamical core, which controls how in- 24 dividual material surfaces are vertically interpolated back to standard pressure levels af- 25 ter each horizontal advection time step. Differences in the age-of-air resulting from changes 26 within the remapping algorithm approach  $\sim 1$  year over the high latitude middle strato- 27 sphere – or about 30% climatological mean values – and imprint on several trace gases, 28 including methane ( $\text{CH}_4$ ) and nitrous oxide ( $\text{N}_2\text{O}$ ). These transport sensitivities reflect, 29 to first order, changes in the strength of tropical upwelling in the lower stratosphere (70- 30 100 hPa) which are driven by changes in resolved wave convergence over northern mid- 31 latitudes as (critical lines of) wave propagation shift in latitude. Our results strongly sup- 32 port continued examination of the role of numerics in contributing to transport biases 33 in composition modeling. 34 35

## 36 Plain Language Summary

37 Large-scale transport plays a crucial role in distributing climatically important trace 38 constituents in the atmosphere, especially in the stratosphere where transport largely 39 determines the chemical lifetimes of trace gases. One summary of transport in the strato- 40 sphere is the “mean age” or the mean transit time since air at a point in the stratosphere 41 was last in the troposphere. Current models used for simulating stratospheric compo- 42 sition produce a range of simulated ages, although these differences are poorly under- 43 stood. Among other factors, model numerics play a critical role in transport, but few 44 studies have explored the sensitivity of the mean age to the choice of numerical scheme 45 employed within different dynamical cores. Here we use one model to show that the mean 46 age is sensitive to the so-called “remapping” algorithm used within the finite-volume dy- 47 namical core that controls how individual material surfaces are vertically interpolated 48 back to standard pressure levels after each horizontal advection time step. This reflects 49 sensitivities in the representation of how waves propagate from the troposphere into the 50 stratosphere. This work suggests that model numerics can be an important factor in con- 51 tributing to differences in simulated transport among models.

## 52 1 Introduction

53 The chemical and radiative properties of the troposphere and lower stratosphere 54 are strongly influenced by the stratosphere-troposphere exchange of mass and tracers (e.g., 55 Morgenstern and Carver (2001); Hegglin et al. (2006); Pan et al. (2007)). Properly sim- 56 ulating the stratospheric circulation and its influence on atmospheric composition in earth 57 system models is important for capturing past decadal trends in surface climate, par- 58 ticularly in response to changes in Southern Hemisphere ozone depletion (e.g., Son et 59 al. (2009); Polvani et al. (2011)). In the Northern Hemisphere (NH), the stratospheric 60 circulation’s coupling to ozone could represent an important feedback on the climate’s 61 response to future increases in greenhouse gases (GHGs), especially over the North At- 62 lantic (e.g., Chiodo and Polvani (2019)). On shorter subseasonal timescales, stratospheric 63 ozone changes associated with strong polar vortex states may also modulate Arctic sea 64 level pressure and surface temperatures (e.g., Ivy et al. (2017); Oehrlein et al. (2020)), 65 so much so that seasonal forecast systems employing prognostic ozone show suggestions

66 of increased signal-to-noise ratio in predictions of the North Atlantic Oscillation (B. M. Monge-  
67 Sanz et al. (2022)).

68 Key to accurately simulating a consistent representation of coupling between strato-  
69 spheric dynamics and chemical trace gases is ensuring that a model’s underlying trans-  
70 port circulation is properly represented. To this end, much effort has been paid to de-  
71 veloping so-called “tracer-independent” metrics of transport (Holzer and Hall (2000))  
72 such as the mean age-of-air (Hall and Plumb (1994)) and to applying these measures to  
73 rigorously evaluate model transport characteristics in chemistry climate models (CCMs)  
74 (e.g., Hall et al. (1999); Orbe et al. (2018); Dietmüller et al. (2018); Abalos et al. (2020)).

75 While the assessment of CCMs participating in the SPARC Chemistry Climate Model  
76 Validation (SPARC CCMVal) effort showed a marked improvement in simulated trans-  
77 port characteristics relative to previous intercomparisons (J. Neu et al. (2010)), more re-  
78 cent analysis of models participating in the SPARC Chemistry Climate Modeling Ini-  
79 tiative (CCMI) (Eyring et al. (2013)) do not demonstrate any improvement (Dietmüller  
80 et al. (2018), see their Figure 3). In particular, although some models produce mean age  
81 values that agree well with observational estimates, the CCMI intermodel spread is  $\sim$   
82 50%, with models generally simulating transport that is too vigorous relative to obser-  
83 vations. While documenting these transport differences among models is straightforward,  
84 understanding the drivers of this spread remains a challenge and there is still no con-  
85 sensus on what is causing the large spread in simulated ages among the current gener-  
86 ation of CCMs.

87 A key challenge in identifying the drivers of age-of-air – and other stratospheric trans-  
88 port – biases is that they reflect the time-integrated effects of advection by the residual  
89 mean circulation and eddy diffusive mixing, or the quasi-random transport due to the  
90 breaking of Rossby waves (e.g., Holton et al. (1995); Plumb (2002)). Given that the in-  
91 fluences of mixing and advection are not easily separable, studies have come to differ-  
92 ent conclusions about sources of age biases in models. In particular, the analysis of the  
93 CCMVal models showed a strong correlation between the intermodel spread in the age-  
94 of-air and lower stratospheric tropical upwelling, whereas Dietmüller et al. (2018) showed  
95 that the age spread among the CCMI models was driven by differences in mixing. While  
96 future attempts to further distinguish between sources of age biases using either simpli-  
97 fied “leaky pipe” models (Plumb (1996); J. L. Neu and Plumb (1999)) or more complete  
98 measures of the transport circulation such as the “age spectrum” (e.g., Hall and Plumb  
99 (1994); Waugh and Hall (2002))) may prove enlightening, at present there is no consen-  
100 sus on what is causing large simulated age-of-air biases in models.

101 One potential limitation of previous work based on multi-model intercomparisons  
102 is that many aspects of model formulation can influence both stratospheric upwelling and  
103 mixing. Thus, while intercomparisons are useful for identifying common model biases,  
104 understanding the drivers of these biases is difficult absent single model-based process  
105 studies. Among these, several aspects of model formulation have been identified as in-  
106 fluencing simulated mean age distributions. As the mean age is sensitive to vertical mo-  
107 tion in the lowermost stratosphere, these include large sensitivities to vertical resolution  
108 (Orbe et al. (2020)) and to spurious vertical mixing either introduced in vertical coor-  
109 dinate transformations in offline chemical transport models (B. Monge-Sanz et al. (2007))  
110 or through use of assimilated winds performed either in offline (e.g., Legras et al. (2004))  
111 or online data assimilation and “nudged” configurations (e.g., Pawson et al. (2007); Orbe  
112 et al. (2017); Davis et al. (2022)). These age sensitivities can be still further amplified,  
113 depending on whether or not parameterized gravity waves are included (Eichinger et al.  
114 (2020)).

115 By comparison, sensitivities of the mean age to underlying tracer numerics have  
116 been less well examined, although Eluszkiewicz et al. (2000) documented a large sensi-  
117 tivity in simulated age-of-air values to the choice of advection scheme. More recently,

118 Gupta et al. (2020) showed differences of  $\sim 25\%$  in the age-of-air across identical exper-  
 119 iments performed using four different dynamical cores, especially between those using  
 120 spectral versus finite-volume schemes. The experiments employed in that study, how-  
 121 ever, were highly idealized and it is not clear if the strong influence of tracer numerics  
 122 that they identified is also realized in more comprehensive model simulations with moist  
 123 physics, especially in the context of model development as carried out in operational mod-  
 124 eling centers.

125 To better elucidate this influence of tracer numerics on the transport properties sim-  
 126 ulated in a comprehensive global model context, here we document the sensitivity of the  
 127 stratospheric mean age in several recent versions of the NASA Global Earth Observing  
 128 System (GEOS) general circulation model (Molod et al., 2015). The versions examined  
 129 here represent different stages in model development since the Modern-Era Retrospec-  
 130 tive Analysis for Research and Applications Version 2 (MERRA-2; Gelaro et al. (2017)).

131 Our focus on transport evaluation is partly in wake of the upcoming release of the  
 132 GEOS Retrospective analysis for the early 21<sup>st</sup> Century (GEOS-R21C), which is an at-  
 133 mospheric reanalysis that includes many advances over MERRA-2, and serves as a step  
 134 towards MERRA-3, a planned coupled Earth system reanalysis. Along with having im-  
 135 plications for GEOS-R21C, our analysis also includes the GEOS-IT Version 5.29.4 dat-  
 136 ing from October 19, 2022 (hereafter simply “GEOS-IT”), which will be used to drive  
 137 an off-line chemistry reanalysis with a full chemistry model (GEOS-Chem) and an ad-  
 138 vanced Constituent Data Assimilation component to update the chemistry fields. Since  
 139 this chemical reanalysis will be produced in replay-mode (one-way coupling) whereby  
 140 the meteorology fields are used to define the background atmospheric flow (Orbe et al.,  
 141 2017), it is imperative that recent tags of GEOS produce a credible representation of trans-  
 142 port processes.

143 In particular, here we document how in the process of evaluating candidate sys-  
 144 tems for GEOS-R21C we found that the mean age was  $\sim 1$  year younger (or  $\sim 30\%$  smaller)  
 145 than the values simulated in the model version used to produce MERRA-2 (Figure 1).  
 146 The model versions shown in Figure 1 reflect more than 10 years’ worth of accumulated  
 147 changes in model development, most notably changes in radiation, parameterized con-  
 148 vection and, as we focus on here, changes in the model’s description of vertical advec-  
 149 tion. More precisely, we show that slight modifications to the so-called “remapping” al-  
 150 gorithm, which is used to transform advected fields from Lagrangian levels to the new  
 151 pressure levels after each horizontal advection time step, are the primary driver of the  
 152 age-of-air changes exhibited in recent GEOS-R21C candidate model versions. Thus, whereas  
 153 Gupta et al. (2020) highlighted large differences between dynamical cores employing spec-  
 154 tral versus finite-volume (FV) numerics, our results show that large transport differences  
 155 can occur even within a given FV dynamical core, a result which may have broader im-  
 156 plications for other general circulation models employing FV numerics. We begin by dis-  
 157 cussing methods in Section 2 and present key results and conclusions in Sections 3 and  
 158 4, respectively.

## 159 2 Methods

### 160 2.1 Model Configurations

161 Here we present results from several versions of GEOS spanning MERRA-2 to more  
 162 recent candidates for GEOS-R21C. Among these model versions, a subset are more “of-  
 163 ficial” as they have been documented and/or employed in recent model intercomparisons  
 164 and are highlighted in Figure 1. In particular, these include a model version that was  
 165 used in Phase 1 of CCM1 and documented in Orbe et al. (2017) (Fig. 1, red line). A more  
 166 recent model version that was used in the CCM1 Phase 2 simulations (correspondence  
 167 with Michael Manyin) is also shown (Fig. 1, green line).

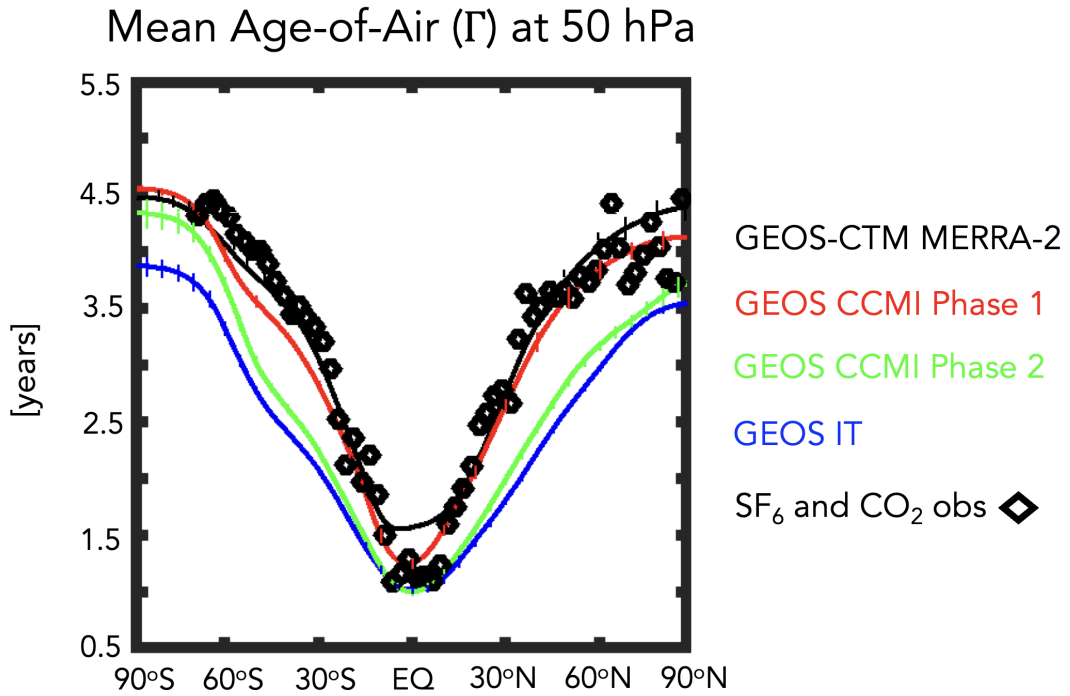


**Figure 1.** The 2000-2010 climatological annual mean meridional profile of the stratospheric mean age-of-air ( $\Gamma$ ), evaluated at 50 hPa. Results from a GEOS-CTM integration constrained with MERRA-2 meteorological fields (black line) as well as free-running GEOS simulations using a model configuration for CCM1 Phase 1 (red line), CCM1 Phase 2 (green line) and the GEOS-IT Version 5.29.4 dating from October 19, 2022 (hereafter simply "GEOS-IT", blue line) are shown. All simulations are constrained with the same (observed) historical sea surface temperatures. Diamonds correspond to SF<sub>6</sub> and CO<sub>2</sub> in situ based estimates of  $\Gamma$  from Boering et al. (1996) and Engel et al. (2009). Vertical dashed lines denote  $\pm\sigma$ , the standard deviation of  $\Gamma$  over 2000-2010, for each model simulation.

168 We begin by comparing 10-year (2000-2010) climatological mean zonally averaged  
 169 age-of-air profiles at 50 hPa across this subset of model versions, derived from 30-year  
 170 long atmosphere-only (AMIP) integrations constrained with observed sea surface tem-  
 171 peratures (Figure 1). First, we note that the profiles for the CCMI Phase 1 version of  
 172 the model are very close to observations (black stars), consistent with the  
 173 “GEOSCCM” documented age characteristics reported in Dietmüller et al. (2018) (see  
 174 their Figure 3). In addition, while passive tracers were not integrated within MERRA-  
 175 2, results using the GEOS chemistry transport model (GEOS-CTM, Kouatchou et al.  
 176 (2015)) constrained with MERRA-2 meteorological fields (black line) also exhibits good  
 177 agreement with observed values. This good agreement between the CTM-generated age-  
 178 of-air and the observations is consistent with results from a previous GEOS-CTM sim-  
 179 ulation (constrained with MERRA) as documented in Orbe et al. (2017).

180 Moving to more recent development versions of the model (green and blue lines),  
 181 however, reveals a reduction in the mean age by  $\sim 1$  year over both southern and north-  
 182 ern high extratropical latitudes, or a decrease of  $\sim 20$ -30% relative to the MERRA-2 con-  
 183 strained simulation and the observations. As discussed earlier, the green line refers to  
 184 the CCMI Phase 2 model version, whereas the blue line refers to GEOS-IT. Note that  
 185 this decrease in the climatological age in both model versions far exceeds the (internal)  
 186 variations in mean age that occur interannually (vertical bars on solid lines).

187 Since MERRA-2, numerous updates have been introduced in the GEOS model. This  
 188 includes replacing the Chou Suarez (Chou & Suarez, 1994) and Chou (Chou, 1990, 1992)  
 189 radiation codes with the Rapid Radiative Transfer Model for GCMs (RRTMG; Iacono  
 190 et al. (2008)), which impacts the stratosphere; the introduction of the Grell-Freitas deep-  
 191 convection code (Grell and Freitas (2014); Freitas et al. (2018)), which has a minimal  
 192 impact on this study; and upgrades to the vertical remapping option from that used in  
 193 MERRA-2 (hereafter denoted as GMAO FV3 Cubic) to the current updated GFDL remap-  
 194 ping option (hereafter denoted as GFDL FV3 Cubic). Note that both MERRA-2 and  
 195 current systems use the GFDL FV3 dynamical core (Lin et al., 2017), but differ in terms  
 196 of this remapping option.

197 As we show in Section 3, the latter transition from the remapping scheme used in  
 198 MERRA-2 (GMAO FV3) to the scheme used in the current GFDL FV3 core has the largest  
 199 impact on the simulated age-of-air values. This degradation in simulated transport within  
 200 the current GFDL FV3 core primarily reflects differences in the implementation of the  
 201 remapping algorithm, which is used to vertically interpolate individual material surfaces  
 202 after each horizontal advection step back to the model’s reference Eulerian coordinate.  
 203 In its implementation in MERRA-2 within the GMAO FV3 core (Table 1), this remap-  
 204 ping involves 1) fitting piecewise parabolic (hereafter PPM) functions to input layer-mean  
 205 values of  $U$ ,  $V$ ,  $Q$  and tracers; 2) calculating PPM functions to output layer edges; 3)  
 206 integrating PPM functions between output layer edges to produce new layer-mean val-  
 207 ues of  $U$ ,  $V$ ,  $Q$  and tracers; 4) calculating total energy (TE) at input mid-layer pressures;  
 208 5) calculating TE at output mid-layer pressures using cubic interpolation and applying  
 209 an a-posteriori integral conservation; and, finally, 6) remapping temperatures from to-  
 210 tal energy via  $T = (TE - K - \Phi)/C_p$ . Here  $T$ ,  $U$ ,  $V$ ,  $Q$ ,  $C_p$ ,  $K$  and  $\Phi$  correspond to tem-  
 211 perature, zonal wind, meridional wind, specific humidity, specific heat capacity and ki-  
 212 netic and potential energy, respectively.

213 Differences in the implementation of this remapping algorithm within the current  
 214 GFDL FV3 core results in degraded simulated stratospheric transport. To demonstrate  
 215 this in as clean a fashion as possible, we use targeted experiments with the GMAO FV3  
 216 system to show that the degradations in simulated transport when using the remapping  
 217 option from the GFDL FV3 core resemble changes that occur when using a lower order  
 218 (quadratic vs. cubic) interpolation scheme in Step 5 of the remapping algorithm (Ta-  
 219 ble 1). This otherwise innocuous change in interpolation order in turn highlights the large  
 220 sensitivities in transport that can occur even *within* a given finite-volume numerical scheme,

**Table 1. GMAO FV3 Core Finite-Volume Remapping Algorithm:** The remapping algorithm examined in this study controls how individual material surfaces are vertically interpolated back to standard pressure levels. Employing linear – and to a lesser extent – quadratic interpolation in Step 5 produces stratospheric transport characteristics that are more consistent with the most recent GEOS model configurations (green and blue lines, Figure 1), whereas a cubic interpolation is more consistent with older configurations (red and black lines, Figure 1) and with MERRA-2. Here  $T$ ,  $U$ ,  $V$ ,  $Q$ ,  $C_p$ ,  $K$  and  $\Phi$  correspond to temperature, zonal wind, meridional wind, specific humidity, specific heat of air at constant pressure and kinetic and potential energy, respectively.

Step	REMAP Procedure (MERRA-2, GMAO FV3 Core)
1	Fit PPM functions to input layer-mean $U$ , $V$ , $Q$ and tracers
2	Calculate PPM to output layer edges
3	Integrate PPM functions between output layer edges to produce new layer-mean $U$ , $V$ , $Q$ and tracers
4	Calculate $TE = C_p T + K + \Phi$ at input mid-layer pressures
5	Calculate $TE$ at output mid-layer pressures using cubic interpolation and a-posteriori integral conservation
6	Construct “remapped” $T$ via $T = (TE - K - \Phi)/C_p$

221 in our case resulting in large differences in lower stratospheric upwelling and a  $\sim 30\%$   
 222 reduction in the simulated mean age of air.

## 223 2.2 Model Experiments

### 224 2.2.1 AMIP vs. EMIP

225 We begin our analysis by interpreting the results shown in Figure 1, which are all  
 226 based on historical AMIPs that were performed at the same cubed sphere C180 (approx-  
 227 imately half-degree) horizontal resolution. As they represent more official model versions  
 228 they serve as an important motivation for the experiments that follow. However, there  
 229 are numerous (potentially compensating) development changes between these model ver-  
 230 sions which renders it nearly impossible to cleanly identify drivers of differences in their  
 231 simulated transport.

232 To this end, in order to investigate the drivers of the differences in Figure 1 we per-  
 233 form targeted modeling experiments aimed at disentangling the influence of individual  
 234 model development changes on stratospheric transport properties (Table 2). In order to  
 235 evaluate impacts on transport climate statistics, we consider both a set of climatolog-  
 236 ical AMIP (rows 1-4) as well as so-called “EMIP” (rows 5-7) experiments.

237 In particular, we carry out 30-year-long AMIP simulations at C180 resolution which  
 238 we use to infer the climate characteristics of the different model configurations. The “EMIP”  
 239 experiments – ensembles of 3-month-long integrations initialized on approximately Novem-  
 240 ber 15 of each year between 1985 and 2015 – are also used to infer impacts on simulated  
 241 transport climate. As they are more computationally efficient than AMIPs since all 30

**Table 2. GEOS Model Experiments:** Targeted GEOS model experiments based off a control experiment (row 1) were carried out to identify the influence of radiation (row 2) and changes in the remapping algorithm used since MERRA-2 (row 3), as well as their combined influence (row 4). The influence of the remapping algorithm changes is then interpreted using a simpler set of sensitivity experiments, performed using the GMAO FV3 core, in which only the order of the interpolation scheme used to calculate TE at output mid-layer pressure levels is altered (rows 5-7). Experiments in rows 1-4 are 30-year-long AMIPs run at C180 resolution, whereas rows 5-7 refer to 30-member 3-month-long (DJF) EMIP experiments. Both AMIPs and EMIPs are used for climate statistic evaluation (see Appendix B for more on the correspondence between the two). EMIP experiments are run at both C180 and C360 horizontal resolutions.

Experiment Name	Configuration	Experiment Type	Hor. Resolution
CTRL	Control, GFDL FV3 Core	AMIP (30 yrs.)	C180
CSRAD	Chou-Suarez (1994) Radiation (RAD)	AMIP (30 yrs.)	C180
M2REMAP	GMAO FV3 Core (cubic)	AMIP (30 yrs.)	C180
CSRAD+M2REMAP	Chou-Suarez (1994) RAD GMAO FV3 Core (cubic)	AMIP (30 yrs.)	C180
LINEAR	GMAO FV3 Core (linear)	EMIP (30 mem.)	C180, C360
QUADRATIC	GMAO FV3 Core (quadratic)	EMIP (30 mem)	C180, C360
CUBIC	GMAO FV3 Core (cubic)	EMIP (30 mem)	C180, C360

242 3-month-long integrations may be run in parallel, they are performed at both C180 and  
 243 C360 (approximately quarter-degree) resolutions in order to examine the sensitivity of  
 244 our results to changes in horizontal resolution.

245 As shown in Appendix B, comparisons of the December-January-February (DJF)  
 246 vertical profile of tropical upwelling show excellent agreement between EMIP and AMIP  
 247 integrations carried out using the same model configuration (Appendix Figure B1). This  
 248 somewhat incidental result represents, to the best of our knowledge, the first time that  
 249 EMIP-based statistics have been shown to converge well to those from AMIPs for the  
 250 stratospheric metrics considered in this study. This suggests that EMIPs, relative to AMIPs,  
 251 may be used to provide a computationally more efficient initial assessment of the impacts  
 252 of model changes on the stratospheric circulation.

### 253 **2.2.2 Model Development Changes**

254 Moving next to the precise model development changes examined, we begin by defin-  
 255 ing a control experiment (CTRL; Table 2, row 1), which best corresponds to the blue  
 256 line shown in Figure 1. Then we define three new AMIP experiments, which aim to dis-  
 257 tinguish between the age-of-air changes resulting from changes in radiation versus changes  
 258 in the handling of the REMAP algorithm that occurred in the transition from MERRA-  
 259 2 to the current FV3 cores (Section 3.2.1).

260 Specifically, these include experiments in which we a) replace RRTMG with the ra-  
 261 diation from Chou and Suarez (1994) (CSRAD; Table 2, row 2), b) replace the current  
 262 FV3 REMAP approach with the settings used in the GMAO FV3 core when running  
 263 MERRA-2 (i.e., M2REMAP; Table 2, row 3) and c) combine these two changes (CSRAD+M2REMAP;  
 264 Table 2, row 4).



As we show in Section 3.2.1, the M2REMAP experiment produces larger changes in age-of-air, compared to the experiment in which only the radiation is altered (CSRAD). Interpreting this result, however, is not straightforward since there are several differences in the implementation of the remapping algorithm between the GMAO and GFDL FV3 cores that are interdependent and, thus, difficult to isolate cleanly. To this end, in order to simplify the problem we focus the remainder of our investigation (Section 3.2.2) on examining a clean set of EMIP experiments that are all performed using the GMAO FV3 core remapping settings and that differ from each other only in terms of the order of the interpolation that is used to calculate TE at the mid-layer pressure levels (Step 5, Table 1). More precisely, we compare configurations using a linear (LINEAR; Table 2, row 5), quadratic (QUADRATIC; Table 2, row 6) and cubic interpolation (CUBIC; Table 2, row 7) scheme, with the latter corresponding to the approach that was used in MERRA-2. To assess the robustness of our findings to changes in horizontal resolution, all three sensitivity experiments are run at both C180 and C360 resolutions.

These three numerical schemes are derived from the generic Lagrangian interpolation equation:

$$\mathcal{Q}(\mathcal{P}) = \sum_{k'} a_{k+k'} \mathcal{Q}_{k+k'} \quad k' = 0, \pm 1, \pm 2, \dots \quad (1)$$

where  $\mathcal{P}$  represents the target output location in  $\ln(p)$  and  $\mathcal{Q}_{k+k'}$  denotes the surrounding grid-point values at input locations. The coefficients  $a_{k+k'}$  are derived through Taylor Series expansions using non-uniform grid spacing given by:

$$a_{k+k'} = \frac{\prod_m (\mathcal{P}_{k+m} - \mathcal{P})}{\prod_m (\mathcal{P}_{k+m} - \mathcal{P}_{k+k'})} \quad m = 0, \pm 1, \pm 2, \dots \quad m \neq k' \quad (2)$$

For the three schemes, the grid points used are: LINEAR ( $k, k-1$ ), QUADRATIC ( $k+1, k, k-1$ ), and CUBIC ( $k+1, k, k-1, k-2$ ). In all cases, the grid points are chosen such that the target location resides between layers  $k$  and  $k-1$ .

Note that, while the LINEAR and QUADRATIC experiments do not actually correspond to any of the model versions shown in Figure 1, they highlight the large sensitivity of the mean age to changes in the interpolation scheme that may otherwise seem innocuous. They also provide further evidence of the strong influence of changes in tropical lower stratospheric upwelling strength on the stratospheric mean age in GEOS.

Finally, in all experiments using the MERRA-2 remapping approach (i.e., M2REMAP, CSRAD+M2REMAP, LINEAR, QUADRATIC, CUBIC) additional modifications to the divergence damping coefficients were used so as to best ensure consistency with what was used in MERRA-2. Specifically, these include changes to the number of layers for vertical subgrid mixing, the coefficient for barotropic mode damping, the use of 2<sup>nd</sup> vs. 6<sup>th</sup> order divergence damping and the strength of the divergence damping coefficients. Compared to the impact of moving from the CTRL to M2REMAP experiments, these additional changes have a much smaller impact on lower stratospheric upwelling in the model (not shown) and hereafter will not be discussed further.

## 2.3 Analysis Approach

### 2.3.1 Transport Diagnostics

To diagnose the transport circulation we focus primarily on the age-of-air (Hall and Plumb (1994)). This is inferred from an idealized global “clock” or ideal age tracer ( $\Gamma$ ) (Thiele and Sarmiento (1990)) that is defined with respect to the bottom model level as follows: initially, the ideal age tracer is set to zero throughout the troposphere and thereafter held to zero over the entire Earth’s surface, subject to a constant aging of 1 year/year throughout the atmosphere. We present here the statistically stationary (equilibrated) value of  $\Gamma(r)$ , which is equal to the average time since the air at a location  $r$

in the stratosphere last contacted the Earth’s surface. In addition to the mean age, we also show results from an idealized e90 tracer that is uniformly emitted over the entire surface layer and decays exponentially at a rate of 90 days<sup>-1</sup> such that concentrations greater than 125 ppb and less than 50 ppb tend to reside in the lower troposphere and stratosphere, respectively (Prather et al. (2011)). As this tracer features strong near-tropopause gradients and takes significantly less time to equilibrate, compared to the mean age, it is useful for evaluating stratosphere-troposphere-exchange and transport within the upper troposphere/lower stratosphere (Abalos et al. (2017, 2020); Orbe et al. (2020)).

Both the mean age and e90 tracers were integrated in all of the AMIP experiments shown in Figure 1 and listed in Table 2 (rows 1-4), which were run using the same idealized passive tracer package described in Orbe et al. (2017). Note that the mean age tracer was not integrated in the EMIP experiments given its much longer characteristic timescale in the stratosphere ( $\sim 3$ -5 years). As such, the EMIP simulations, which do not exceed one year, are not appropriate for evaluating the time-integrated transport characteristics reflected in the age-of-air.

In addition to carrying the idealized tracers, two of the experiments shown in Figure 1 were also run with full interactive chemistry and correspond to the two CCMI (Phase 1 and Phase 2) integrations (red and green lines, Figure 1). Both simulations employ the same Global Modeling Initiative (GMI) chemical mechanism (Strahan et al. (2013)) and are therefore useful in evaluating the impact of age differences on real trace gas distributions. In particular, as shown in Section 3.1 results from these experiments show significant imprints of the age-of-air changes on nitrous oxide (N<sub>2</sub>O) and methane (CH<sub>4</sub>).

### 2.3.2 Circulation Diagnostics

As we show in Section 3, the changes in age-of-air across the different model versions are strongly tethered to changes in the advective component of the circulation, which we quantify using the Transformed Eulerian Mean (TEM) estimate of the Lagrangian transport of mass by the circulation. Thus, in addition to more standard Eulerian metrics of the circulation (e.g., zonal winds and temperatures), we focus on the vertical component of the TEM residual velocity, defined as  $\bar{w}^* = \bar{w} + \frac{\partial(\psi \overline{\cos\phi})}{\partial\phi}$ , where  $\psi = \overline{v'\theta'}/\frac{\partial\theta}{\partial p}$  is the eddy stream function,  $\theta$  refers to potential temperature,  $a$  is the Earth’s radius and overbars and primes denote zonal means and deviations therefrom, respectively (Andrews et al. (1987)). In addition, we interpret the behavior in  $w^*$  using the Eliassen-Palm flux divergence ( $\nabla \cdot \mathbf{F}$ ), whose horizontal ( $\mathbf{F}(\phi)$ ) and vertical ( $\mathbf{F}(p)$ ) components are respectively defined as  $\mathbf{F}(\phi) = a \cos\phi [\frac{\partial u}{\partial p} \psi - \overline{u'v'}]$  and  $\mathbf{F}(p) = a \cos\phi ([f - \frac{\partial u \cos\phi}{\partial\phi}] \psi - \overline{u'\omega'})$ .

## 2.4 Observations and Reanalyses

While our focus is on interpreting and understanding the different model configurations, we incorporate observations to provide context when possible, although we do not present an exhaustive evaluation of the model’s transport characteristics (for that see earlier studies including Orbe et al. (2017, 2018)). However, as the tracers are not directly integrated in MERRA-2 (with the exception of ozone), we compare against independent observational estimates. For the mean age we first compare simulated meridional age profiles at 50 hPa with values derived from in situ aircraft measurements of carbon dioxide (CO<sub>2</sub>), averaged in 2.5 degree latitude bins over the altitude range 19.5 to 21.5 km (Boering et al. (1996), see also Figure 5 in Hall et al. (1999)).

We also briefly evaluate impacts of transport biases on the simulated trace gas distributions for the CCMI Phase 1 and 2 experiments. The simulated fields of methane (CH<sub>4</sub>) are compared with the climatologies derived for 1991–2002 from the Halogen Occultation Experiment (HALOE) on board the Upper Atmosphere Research Satellite (UARS) (Groß and Russell III (2005)). Comparisons of simulated nitrous oxide (N<sub>2</sub>O) are made

### DJF Climatological Mean Tropical Upwelling ( $w^*$ )

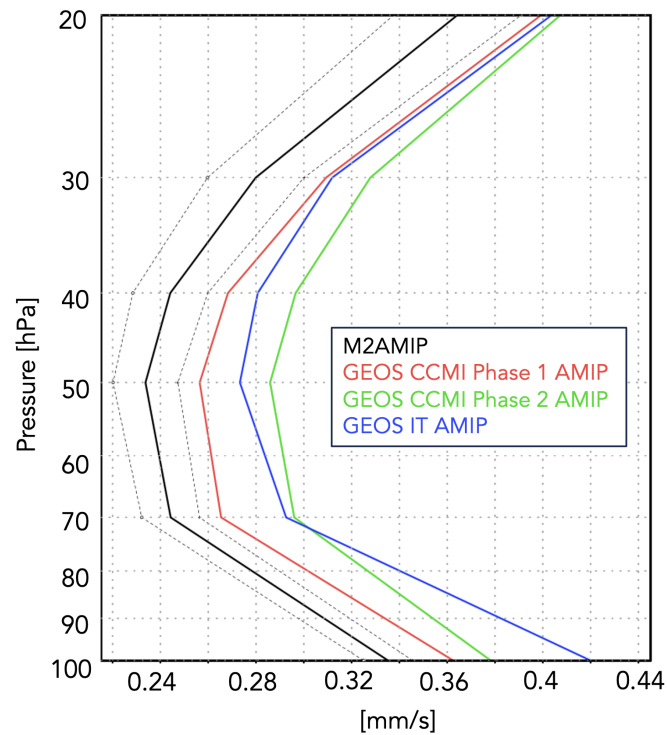


**Figure 2.** The DJF 1985-1994 climatological mean vertical residual mean velocity,  $w^*$ , averaged at each level between the turnaround latitudes for GEOS free-running AMIP simulations using the model configurations corresponding to the CCM1 Phase 1 (red) and Phase 2 (green) submissions and to GEOS-IT (blue). M2AMIP is shown in black, with black dashed lines denoting  $\pm 1$  standard deviation.

359 against climatologies derived from the Microwave Limb Sounder (MLS) on the Earth Ob-  
 360 serving System (EOS) Aura satellite. Climatologies over the same period (2005–2015)  
 361 are used to evaluate both the model and the observations. We use the 190-GHz retrieval  
 362 from Version 4.2 because the 640-GHz data set ends in summer 2013 due to the failure  
 363 of the N<sub>2</sub>O primary band.

364 For the circulation diagnostics nearly all comparisons are made relative to the MERRA-  
 365 2 data assimilation (DAS) reanalysis product, noting that comparisons against ERA-5  
 366 (not shown) reveal a similar picture. One exception, however, is the vertical component  
 367 of the TEM circulation ( $w^*$ ), which shows some differences in vertical structure between  
 368 the MERRA-2 DAS and a 30-member ensemble of (free-running) AMIP integrations pro-  
 369 duced using the MERRA-2 model, hereafter referred to as M2AMIP (Collow et al., 2017)(Ap-  
 370 pendix Figure A1, right). As the free-running model results shown in Figure 1 show more  
 371 consistency with the vertical profile of M2AMIP, not MERRA-2, we compare  $w^*$  in all  
 372 free-running GEOS experiments with M2AMIP, noting that for non-derived measures  
 373 (i.e., winds, temperatures), the raw MERRA-2 output is used.

374 The differences in  $w^*$  between M2AMIP and the MERRA-2 DAS may reflect the  
 375 influence of temperature increments in the DAS (MERRA-2) which can drive spurious  
 376 vertical transport in assimilated products (Weaver et al., 1993; Orbe et al., 2017). In par-  
 377 ticular, Weaver et al. (1993) showed that the imbalance between the thermal and veloc-  
 378 ity fields at the time an observation is ingested during the assimilation cycle can excite  
 379 unwanted inertial-gravity wave modes that manifest strongly in the residual vertical winds.  
 380 While this impact of the increments may explain the differences in  $w^*$ , we reserve a more-  
 381 in depth examination for future work as our focus is on the transport characteristics of  
 382 the free-running GEOS system.

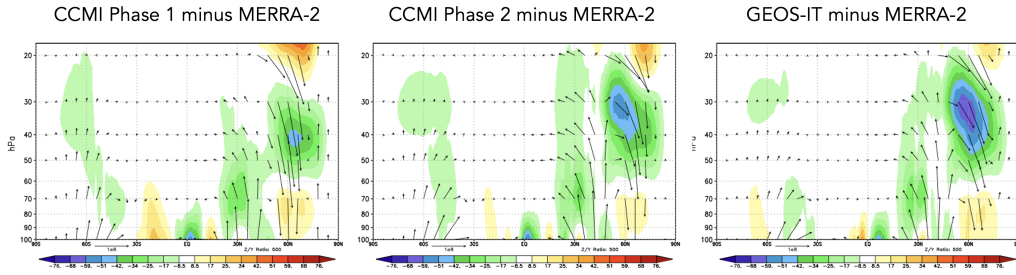
### 383 3 Results

#### 384 3.1 Reduction of Stratospheric Mean Age in GEOS Models 385 Since MERRA-2

386 We begin by interpreting the reduction in mean age exhibited in more recent model  
 387 versions in terms of changes in the strength of upwelling in the tropical lower stratosphere.  
 388 In particular, the reductions in  $\Gamma$  (Figure 1) are consistent with increases in the strength  
 389 of lower stratospheric tropical upwelling, with  $w^*$  becoming progressively stronger in more  
 390 recent model versions, relative to MERRA-2 (Figure 2). Note that these increases in  $w^*$   
 391 across model versions exceed those due to internal variability alone (black dotted lines,  
 392 Fig. 2). Furthermore, while the increases in  $w^*$  occur throughout the stratosphere, we  
 393 focus on the changes occurring between 70 and 100 hPa as these are most relevant to  
 394 determining the tropical upward mass flux and associated strength of the mean overturn-  
 395 ing circulation.

396 Though perhaps naive, the relationship between lower stratospheric upwelling and  
 397 the mean age suggested by comparing Figure 1 and Figure 2 is consistent with the long-  
 398 term behavior of  $\Gamma$  inferred from both historical and projected future climate simulations  
 399 (Butchart et al. (2010); Abalos et al. (2021)). A strong relationship between the strength  
 400 of lower stratospheric ascent and the mean age was also shown to hold in the CCMVal  
 401 models (see Fig. 5.20 in J. Neu et al. (2010)). Nevertheless, it is important to note that  
 402 a clear relationship between  $w^*$  and  $\Gamma$  is not a priori expected, as the age-of-air is also  
 403 known to be very sensitive to mixing, which may be important in interpreting differences  
 404 among the CCM1 Phase 1 models (Dietmüller et al. (2018)).

405 The differences in  $w^*$  highlighted in Figure 2 are associated with enhanced Eliassen-  
 406 Palm flux convergence over NH midlatitudes (Figure 3). Increased wave convergence is  
 407 evident not only within the subtropical lower stratosphere ( $< 30^\circ\text{N}$ , 50-100 hPa) but also  
 408 over higher latitudes and altitudes ( $\sim 40^\circ\text{-}70^\circ\text{N}$ , 20-50 hPa). The fact that differences

DJF Climatological Mean Eliassen-Palm Flux Divergence ( $\nabla \cdot \mathbf{F}$ )

**Figure 3.** Colors show anomalies in the DJF climatological mean Eliassen-Palm (EP) flux divergence between the CCMI Phase 1 (left), CCMI Phase 2 (middle) and GEOS-IT AMIP (right) model versions, relative to MERRA-2. Arrows denote anomalies in the vertical and meridional EP flux vectors (relative to MERRA-2).

409 in extratropical wave convergence imprint on tropical upwelling is consistent with our  
 410 understanding of the so-called “downward control” principle (Haynes et al. (1991)).

411 In particular, the strength of the residual mean streamfunction ( $\Psi^*$ ) is, via down-  
 412 ward control, directly related to the vertically integrated eddy-induced total zonal force  
 413 above that level and has contributions both from the (resolved wave) Eliassen-Palm flux  
 414 divergence (Figure 3) as well as the gravity wave drag scheme’s parameterized waves (not  
 415 shown). The tropical upward mass flux – defined as  $\Psi_{\max}^* - \Psi_{\min}^*$  evaluated at the turnaround  
 416 latitudes (e.g. Rosenlof (1995)) – is therefore directly dependent on the wave forcing aloft.

417 One subtlety to note is that the wave convergence changes shown in Figure 3 oc-  
 418 cur at high latitudes and are directly associated with downwelling over the polar region.  
 419 It is then via mass balance that anomalously strong downwelling associated with enhanced  
 420 flux convergences must be accompanied by enhanced upwelling in the tropics. This in-  
 421 direct impact of higher latitude wave drag reflects an “extratropical pumping” mecha-  
 422 nism (Holton et al., 1995), which is illustrated more clearly in Section 3.2.2 in the con-  
 423 text of the LINEAR, QUADRATIC and CUBIC experiments.

424 While the reduction in  $\Gamma$  (Figure 1) of  $\sim 30\%$  at 50 hPa is significant, it is neither  
 425 clear if this change is representative of other altitudes within the stratosphere nor how  
 426 this age bias imprints on real chemical species. To this end, we begin by comparing the  
 427 full latitude-pressure distribution of changes in  $\Gamma$  and another passive tracer (e90) (Fig-  
 428 ure 4) between the CCMI Phase 1 and Phase 2 model configurations (red and green lines,  
 429 Figure 1). In particular, we find that the changes in both passive tracers – large reduc-  
 430 tions in  $\Gamma$  within both hemispheres (Fig. 4, top right) and increased values of e90 within  
 431 the lower stratosphere (Fig. 4, bottom right) – are reflective of an overall increase in the  
 432 strength of the transport circulation. This is highlighted in the CCMI Phase 2 – 1 model  
 433 differences for the passive tracer distributions (Fig. 4, right panels) which are shown in  
 434 the absence of robust observational constraints of  $\Gamma$  at higher altitudes (or any obser-  
 435 vational constraints for e90, for that matter). The reduced/increased stratospheric bur-  
 436 dens of the age and e90 tracers are consistent with stronger upwelling in the CCMI Phase  
 437 2 model configuration (Figure 2).

438 While the observational constraints on  $\Gamma$  presented in Figure 1 and the departure  
 439 of  $w^*$  away from MERRA-2 suggest that transport properties of the newer model con-  
 440 figurations are moving in the wrong direction, it is relevant to ask whether or not the

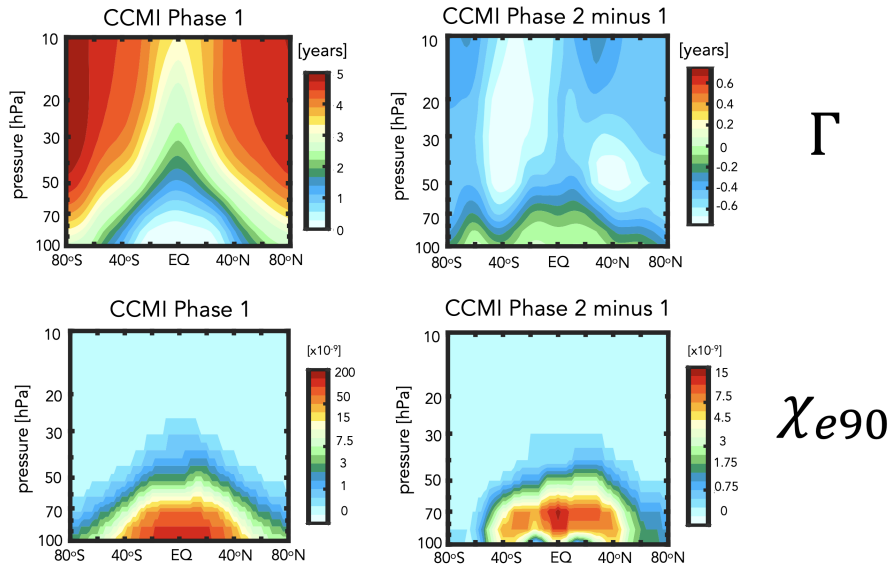


**Figure 4.** The climatological mean (2000-2010) distribution of the mean age-of-air ( $\Gamma$ ) (left, top) and e90 idealized tracers (left, bottom) for the CCMI Phase 1 model configuration. Climatological differences between the CCMI Phase 2 and Phase 1 model configurations are shown in the right panels. Note that a nonlinear colorbar has been used in the e90 subplots.

441 trace gas satellite measurements also support this conclusion. Indeed, comparisons with  
 442 observations show larger biases in  $\text{N}_2\text{O}$  (Fig. 5, top panels) and  $\text{CH}_4$  (Fig. 5, bottom pan-  
 443 els), increasing from 10% to 30% in the CCMI Phase 2 model configuration, depending  
 444 on the species. Recall that the same chemistry mechanism is used in both CCMI Phase  
 445 1 and 2 simulations.

446 The patterns of the trace gases biases are generally consistent with the biases in  
 447 the mean age (Fig. 4). This comports with well-known correlations between the mean  
 448 age and stratospheric trace gases, reinforcing the fact that model transport inaccuracies  
 449 can significantly affect simulations of important long-lived chemical species in the strato-  
 450 sphere (Hall et al. (1999)).

451 The fact that the mean age changes have a significant imprint on the simulated trace  
 452 gases is consequential for the GEOS-R21C system. However, the configurations shown  
 453 in Fig. 1-5 differ in many respects (physics, resolution, radiation, FV remapping algo-  
 454 rithm) and it is difficult to meaningfully interpret what is driving the changes in  $w^*$  (and  
 455 the tracers). We therefore move next to the targeted model experiments (Table 2) in or-  
 456 der to interpret the model development steps that resulted in these transport circula-  
 457 tion changes.

### 458 **3.2 Identifying Drivers of Upwelling and Tracer Changes Since** 459 **MERRA-2**

#### 460 **3.2.1 Radiation versus REMAP Algorithm**

461 As discussed in Section 2, among the model changes that were made since MERRA-  
 462 2, the changes in radiation and the FV remapping algorithm are most likely to directly  
 463 have impacted the stratospheric circulation. We therefore begin by assessing which of  
 464 these changes dominates the decreases in  $\Gamma$  shown in Figure 1.

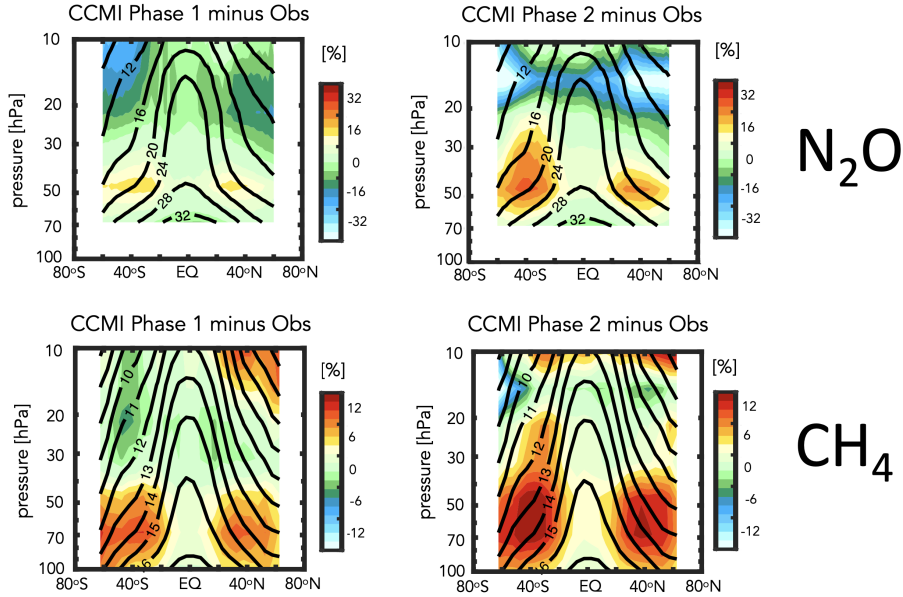


**Figure 5.** Colors shown anomalies in the simulated distributions of nitrous oxide ( $\text{N}_2\text{O}$ ) (top) and methane ( $\text{CH}_4$ ) (bottom), relative to the MLS and HALOE observed values, respectively, for the CCMI Phase 1 (left) and Phase 2 (right) GEOS model configurations. Climatological mean observed values are shown in the black contours.

465 Figure 6 shows the distribution of  $\Gamma$  for experiments in which the longwave, short-  
 466 wave, and REMAP updates since MERRA-2 have successively been undone. Relative  
 467 to the control experiment (CTRL; Table 2, row 1), the transition back to Chou and Suarez  
 468 (1994) in the shortwave and Chou (1990, 1992) in the longwave results in an increase in  
 469 the mean age of  $\sim 0.5$  years throughout the stratosphere (CSRAD; Table 2, row 2). Though  
 470 significant, this change in  $\Gamma$  is smaller than the change that results from applying the  
 471 remapping approach used in MERRA-2 (M2REMAP; Table 2; row 3), in which the mean  
 472 age increases by  $\sim 1$  year. The combined impacts of both changes (CSRAD+M2REMAP;  
 473 Table 2 row 4) is roughly linear, with age values of  $\sim 5.5$  years over high latitudes at 50  
 474 hPa, consistent with the values simulated by the GEOS-CTM MERRA-2 integration (black  
 475 line, Figure 1) and with the CCMI Phase-1 version of the model (red line, Figure 1).

476 Next we ask if the behavior of  $\Gamma$  exhibited in Figure 6 can be interpreted in terms  
 477 of changes in the strength of lower stratospheric tropical upwelling and extratropical wave  
 478 convergence, as our previous analysis of the CCMI experiments suggested. Indeed, Fig-  
 479 ure 7 shows that values of upwelling decrease in the CSRAD and M2REMAP experiments,  
 480 relative to the CTRL integration. The increase in upwelling resulting from both changes  
 481 (CSRAD+M2REMAP) is still larger, consistent with the larger age decreases in that ex-  
 482 periment. This change in the behavior of  $w^*$  within the tropical stratosphere can be in-  
 483 terpreted in terms of changes in the Eliassen Palm flux convergence over NH midlati-  
 484 tudes (not shown), which features smaller values in the CSRAD, M2REMAP (and CSRAD+  
 485 MSREMAP) experiments. Note that our examination of the changes in  $w^*$  are derived  
 486 from EMIP integrations, which we showed previously converge (for DJF) to the statis-  
 487 tics derived from corresponding AMIP experiments.

488 It is important to note that, while the reduced values of  $w^*$  in the M2REMAP ex-  
 489 periment (Fig. 7), represent an improvement, relative to the CTRL integration, these

### Annual Climatological Mean Stratospheric Mean Age ( $\Gamma$ )

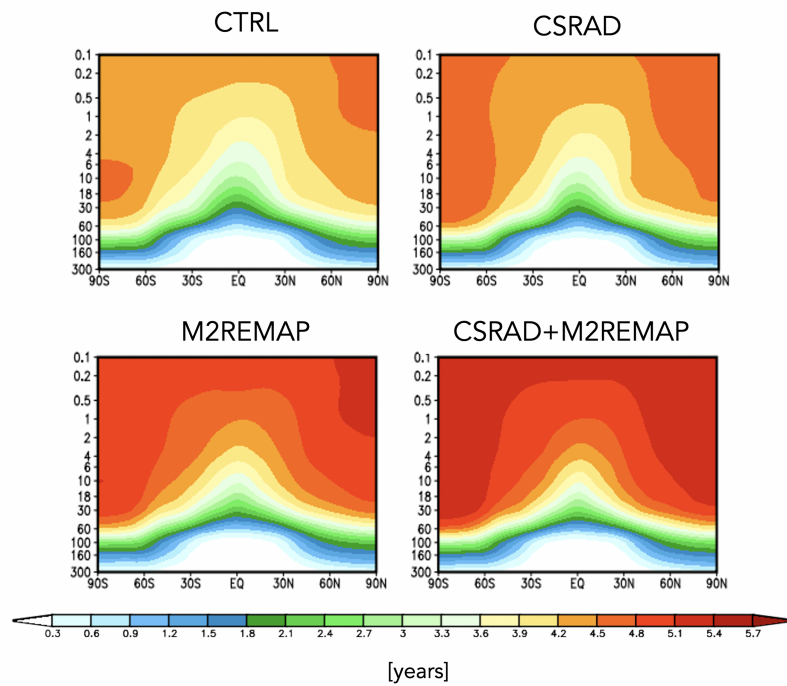


**Figure 6.** Colors show the simulated 2000-2010 climatological annual mean distributions of the mean age-of-air ( $\Gamma$ ) for the CTRL (top left; Table 2, row 1), CSRAD (top right; Table 2, row 2), M2REMAP (bottom left; Table 2, row 3) and combined CSRAD+M2REMAP (bottom right; Table 2, row 4) experiments.



490 changes are, in isolation, accompanied by a cold bias ( $\sim 4-6$  K) in the tropical lower strato-  
 491 sphere (Fig. 8a). Unlike the upwelling changes, this represents a degradation in model  
 492 skill, increasing the temperature bias in that region, relative to MERRA-2 (Fig. 8 b,c).  
 493 While this temperature bias is concerning in isolation, it is decoupled from the changes  
 494 in residual mean upwelling which, rather, are more sensitive to the changes in *extratrop-*  
 495 *ical* wave convergences (described further in the next section). Furthermore, the increased  
 496 temperature bias in the M2REMAP experiment appears to be tethered to other updates  
 497 that were made in the CTRL model (specifically the radiation progression from Chou-  
 498 Suarez to RRTMG). In particular, the M2AMIP ensemble, which also employs the GMAO  
 499 cubic remapping option, features a much smaller temperature bias in the tropical lower  
 500 stratosphere, relative to MERRA-2 ( $\sim 0-2$ K) (Fig. 8d). This suggests that the ampli-  
 501 fied temperature bias moving from the CTRL to M2REMAP experiments needs to be  
 502 interpreted in the context of other model development changes that were introduced, par-  
 503 ticularly in the radiation scheme and its coupling to convection.

### 504 **3.2.2 FV REMAP Algorithm: Sensitivity of Climate Statistics**

505 Having shown in the previous section that the largest changes in the mean age were  
 506 realized through the differences in implementation of the remapping algorithm between  
 507 the GMAO FV3 core used in MERRA-2 and in current FV3 core configurations, we now  
 508 investigate further the sensitivity of the transport circulation to the choice of remapping  
 509 interpolation scheme. In particular, we compare simulations run with the GMAO FV3  
 510 remapping settings in which total energy is calculated at new mid-layer pressures using  
 511 cubic, quadratic and linear interpolation prior to the aposterior integral conservation (Ta-  
 512 ble 2, rows 5-7). In addition, in this section we seek to understand how the changes in  
 513 the Eliassen-Palm flux convergence over NH midlatitudes arise via analysis of the large-  
 514 scale wind structure.

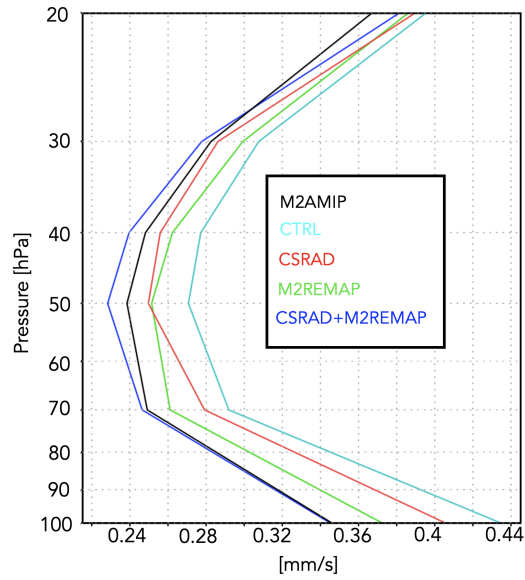
515 Figure 9 (left panel) shows a clear sensitivity in tropical upwelling to the choice of  
 516 interpolation scheme, with  $w^*$  progressively increasing in strength moving from the CU-  
 517 BIC to QUADRATIC to LINEAR schemes. This sensitivity is robust across horizontal  
 518 resolutions as the same suite of experiments performed at C360 exhibit the same sensi-  
 519 tivity (Fig. 9, right panel). While no current model version actually employs a linear  
 520 scheme, this suite of experiments highlights the strong sensitivity to choice of interpo-  
 521 lation scheme within the remapping algorithm; to the best of our knowledge, this result  
 522 has not been reported in the literature.

523 Furthermore, as we show next, this clean set of experiments allow us to inquire mech-  
 524 anistically into the processes that are driving the changes in wave convergence over mid-  
 525 latitudes, unencumbered by differences in horizontal resolution, physics, etc.

526 Interestingly, the increases in  $w^*$  moving from the CUBIC to QUADRATIC schemes  
 527 not only manifests in free-running AMIP simulations, but also in AMIP simulations in  
 528 which GEOS is constrained (or replayed, following Orbe et al. (2017)) to MERRA-2 me-  
 529 teorological fields, using the MERRA-2 GMAO cubic interpolation (Fig. 10, blue line)  
 530 and the GFDL FV3 core remapping approach (Fig. 10, red line). While there is a gen-  
 531 eral increase in  $w^*$  in the former, however, both simulations, lie within the range of MERRA2-  
 532 DAS, suggesting that replay does act to ameliorate some of the upwelling biases man-  
 533 ifest in the underlying unconstrained models. While not the focus of this study, this im-  
 534 pact of the remapping approach on simulations run in replay mode will be examined fur-  
 535 ther in future work.

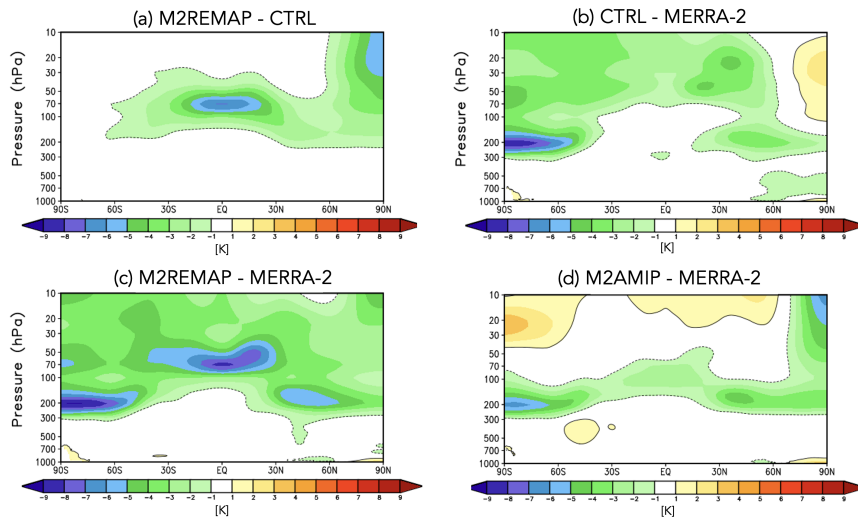
536 Consistent with our expectations based on the analysis of the previous experiments,  
 537 the drivers of the changes in  $w^*$  are related to increased wave convergence moving from  
 538 the CUBIC to QUADRATIC to LINEAR schemes (Figure 11). Over extratropical lat-  
 539 itudes, the zonal force associated with this enhanced wave convergence is associated with  
 540 enhanced downwelling at high latitudes that, through mass balance, is accompanied by

DJF Climatological Mean Tropical Upwelling ( $w^*$ )



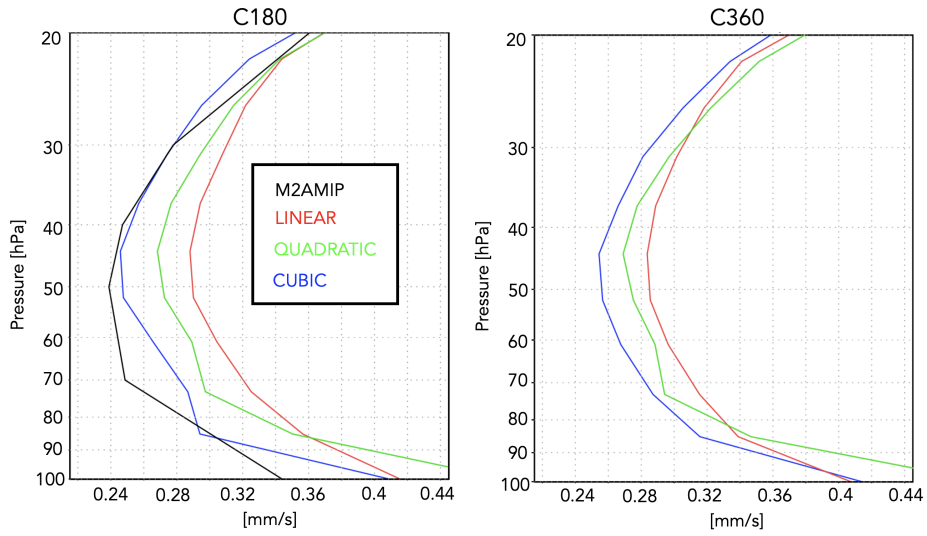
**Figure 7.** The DJF 1985-2015 climatological mean vertical residual mean velocity,  $w^*$ , averaged at each level between the turnaround latitudes for the CTRL (cyan line; Table 2, row 1), CSRAD (red line; Table 2, row 2), M2REMAP (green line; Table 2, row 3) and combined CSRAD+M2REMAP (blue line; Table 2, row 4) experiments. M2AMIP is shown in black.

DJF Climatological Zonal Mean Temperature Anomalies



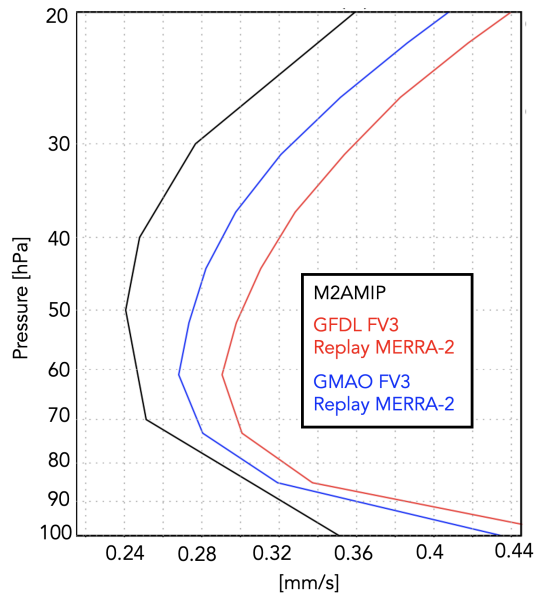
**Figure 8.** Anomalies in DJF 1985-2015 climatological mean zonal mean temperatures: M2REMAP - CTRL (a), CTRL - MERRA-2 (b), M2REMAP - MERRA-2 (c) and M2AMIP - MERRA-2 (d).

### DJF Climatological Mean Upwelling ( $w^*$ )

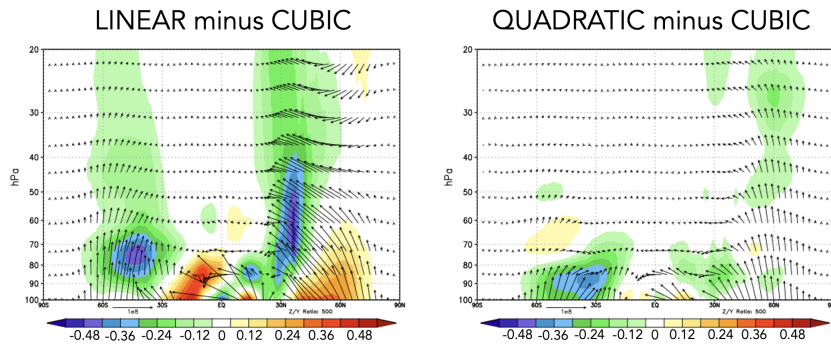


**Figure 9.** The DJF 1985-2015 climatological mean vertical residual mean velocity,  $w^*$ , averaged at each level between the turnaround latitudes for the LINEAR (red line; Table 2, row 5), QUADRATIC (green line; Table 2, row 6) and CUBIC (blue line; Table 2, row 7) experiments. M2AMIP is shown in black. Results from C180 and C360 EMIP experiments are shown in the left and right panels, respectively.

### DJF Climatological Mean Tropical Upwelling ( $w^*$ )



**Figure 10.** The DJF 2005-2015 climatological mean vertical residual mean velocity,  $w^*$ , averaged at each level between the turnaround latitudes for two GEOS replay AMIP simulations constrained with MERRA-2 meteorological fields using remapping approaches from the MERRA-2 GMAO FV3 cubic core (blue line) and the GFDL FV3 core (red line). MERRA-2 DAS is shown in black.

DJF Climatological Mean Eliassen-Palm Flux Divergence ( $\nabla \cdot \mathbf{F}$ )

**Figure 11.** Colors shown anomalies in the DJF 1985-2015 climatological mean Eliassen-Palm (EP) flux divergence in the LINEAR (left) and QUADRATIC (right) experiments, relative to the CUBIC model experiment. Arrows denote anomalies in the vertical and meridional EP flux vectors.

541 enhanced upwelling in the tropics. This indirect impact of higher latitude wave drag is  
 542 evident in Appendix Figure C1, which shows stronger upwelling/downwelling in the LIN-  
 543 EAR and QUADRATIC experiments over the tropics/polar region.

544 Next we exploit the fact that these experiments only differ with respect to the in-  
 545 terpolation scheme in order to inquire further into the drivers of the wave convergence  
 546 changes. To this end, Figure 12 compares profiles of the zonal mean zonal wind between  
 547 the CUBIC, QUADRATIC and LINEAR experiments, averaged over the region of en-  
 548 hanced wave convergence (i.e. 20°N-60°N). The experiments featuring stronger wave con-  
 549 vergence (LINEAR and QUADRATIC) are also simulations with stronger zonal winds,  
 550 relative to MERRA-2, especially above 70 hPa. This change in winds occurs at both C180  
 551 (Fig. 12, left panel) and C360 (Fig. 12, right panel) resolutions.

552 Structurally, the increase in zonal wind strength over northern extratropical mid-  
 553 latitudes is reflective of a poleward shift in the zonal winds as the critical latitude, i.e.  
 554 where the zonal wind is zero, shifts northward in the QUADRATIC and, especially, LIN-  
 555 EAR integrations, relative to the CUBIC experiment (Figure 13). Since stationary waves  
 556 only propagate in westerly zonal flow, the latitude where zonal flow is zero acts a bound-  
 557 ary for wave propagation (Hardiman et al. (2014)). As a result, this shift in critical lat-  
 558 itude results in enhanced wave propagation and convergence over middle and high lat-  
 559 itudes.

560 Figures 12 and 13 highlight how the changes in zonal winds in the LINEAR and  
 561 QUADRATIC experiments reflect a degradation in model skill, relative to MERRA-2,  
 562 throughout the entire stratosphere. The changes in upwelling, mean age, chemical trace  
 563 gases and zonal winds thus provide a coherent and self-consistent picture suggestive of  
 564 a degradation in the representation of the stratospheric circulation since MERRA-2. That  
 565 is, an increased bias in the stratospheric northern zonal winds are, via their influence on  
 566 wave convergence, compromising changes in the strength of the mean meridional over-  
 567 turning circulation and its impact on composition. It is interesting to note that the wind  
 568 biases also extend into the troposphere and show degraded skill relative to MERRA-2  
 569 in the LINEAR and QUADRATIC experiments (Figure 13). Examination of other fields

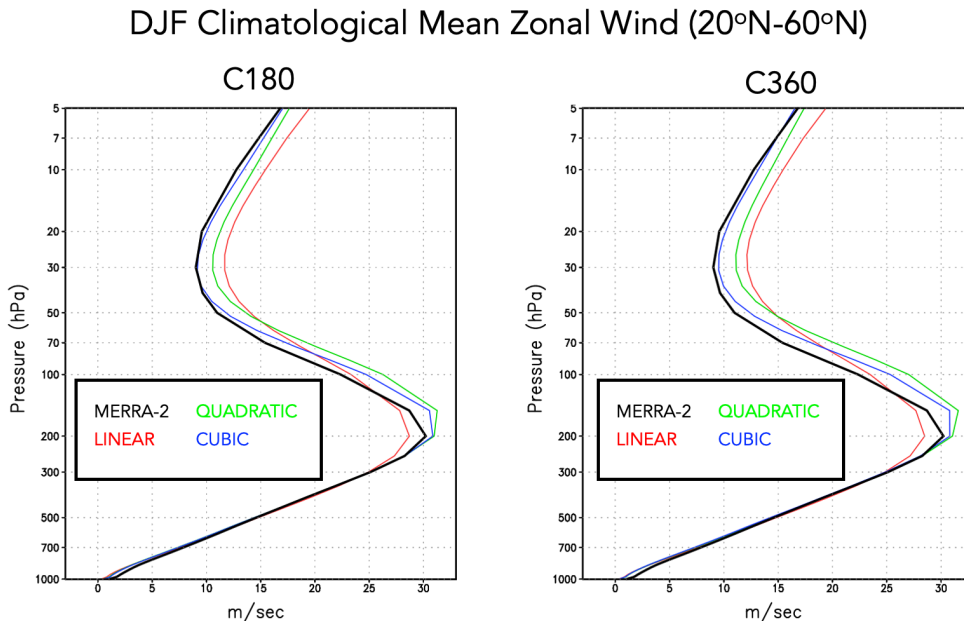


**Figure 12.** Vertical profiles of the DJF 1985-2015 climatological mean zonal mean zonal winds in the LINEAR (red), QUADRATIC (green) and CUBIC (blue) experiments, averaged between 20°N and 60°N. MERRA-2 is shown in the black line. Results for both C180 (left) and C360 (right) experiments are shown.

570 (i.e. tropopause biases, Appendix Figure D1) present somewhat more of a nuanced story  
 571 that depends on other changes that made to the model since MERRA-2, as shown in Fig-  
 572 ure 8 and discussed in Section 3.2.1. The improvements in the zonal winds, however, are  
 573 most relevant for setting the upwelling characteristics within the tropical lower strato-  
 574 sphere via their influence on wave propagation into that region.

575 Finally, to better understand why these impacts on the winds have such a conse-  
 576 quence for the wave convergence properties within the stratosphere, next we examine the  
 577 zonal structure of these biases in the middle stratosphere (Figure 14. This reveals that  
 578 the enhanced winds in the LINEAR (and, to a lesser extent, QUADRATIC) integrations  
 579 are concentrated over the North Pacific at both C180 (Fig. 14, top) and C360 (Fig. 14,  
 580 bottom) resolutions (a similar picture emerges within the troposphere, not shown). As  
 581 this region is the primary region dominating the stationary component of the upward  
 582 flux of vertical wave activity (Plumb (1985), see their Figure 4) it is perhaps not surpris-  
 583 ing that this region is having a profound impact on the mean overturning circulation.  
 584 Again, as with the zonal mean wind changes, the increases in wind strength over the North  
 585 Pacific represent degraded model skill relative to MERRA-2. Note that comparisons with  
 586 ERA-5 reveal a similar bias (not shown).

## 587 4 Conclusions

588 Here we have performed an analysis aimed at understanding differences in the repre-  
 589 sentation of the stratospheric circulation in recent candidate systems for GEOS-R21C,  
 590 relative to older versions of GEOS similar to the model used to produce MERRA-2. Us-  
 591 ing targeted experiments oriented at disentangling various model development updates,  
 592 we have identified a key role played by changes in the implementation of the remapping

## DJF Climatological Zonal Mean Zonal Wind Anomalies Relative to MERRA-2

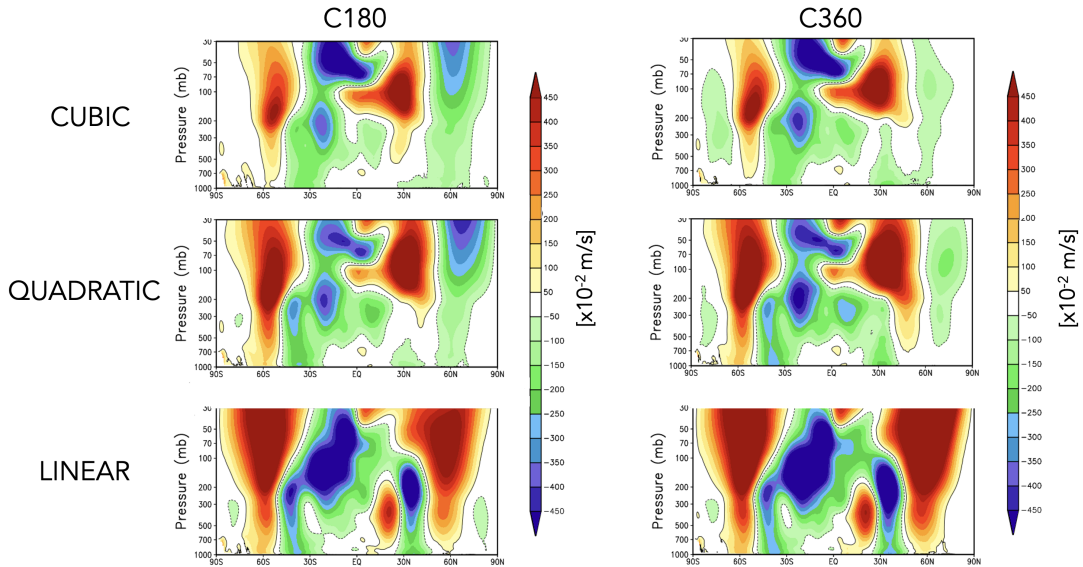


**Figure 13.** Colors shown anomalies in the DJF 1985-2015 climatological mean zonal mean zonal winds in the CUBIC (top), QUADRATIC (middle) and LINEAR (bottom) experiments, relative to MERRA-2. Results for both C180 (left) and C360 (right) experiments are shown.

593 algorithm within the model’s finite-volume dynamical core. Our key results are as fol-  
 594 lows:

595 #1. The stratospheric mean age-of-air in GEOS is sensitive to the degree of the  
 596 interpolation scheme that is used to calculate layer-mean values of total energy,  $U$ ,  $V$  and  
 597 tracers. Different treatment of the vertical remapping algorithm result in mid-stratospheric  
 598 (50 hPa) age-of-air differences of  $\sim 1$  year over high latitudes, or about 30% climatolog-  
 599 ical mean values.

600 #2. The increased age-of-air biases in more recent GEOS configurations are reflected  
 601 in the increased biases in simulated trace gases, including  $\text{CH}_4$  and  $\text{N}_2\text{O}$ .

602 #3. The age-of-air sensitivities reflect, to first order, changes in the strength of trop-  
 603 ical upwelling associated with the Brewer-Dobson circulation which are in turn are driven  
 604 by changes in EP flux convergence over northern midlatitudes. Changes in wave conver-  
 605 gence reflect shifts in (critical lines of) wave propagation that originate in the troposphere  
 606 over the Pacific Ocean, a region of strong upward wave activity.

607 #4. The degradation of upwelling statistics manifest in AMIPs, also translate to  
 608 degradations in configurations of GEOS in which the meteorological fields are constrained  
 609 or “replayed” to MERRA-2.

610 An important caveat should be mentioned in relation to Conclusion 3 listed above,  
 611 which highlights the leading role played by *extratropical* wave convergences in the be-  
 612 havior of tropical upwelling in the model. While this is consistent with our understand-  
 613 ing that the Brewer-Dobson Circulation is, to first order, determined by extratropical  
 614 wave flux convergences, in practice this means that other undesirable biases may emerge  
 615 in the tropics (i.e., tropical temperatures, Figure 8). Our analysis of the M2AMIP en-  
 616 semble, however, suggests that this tropical temperature bias is not a necessary conse-

### DJF Climatological 30 hPa Zonal Wind Anomalies Relative to MERRA-2

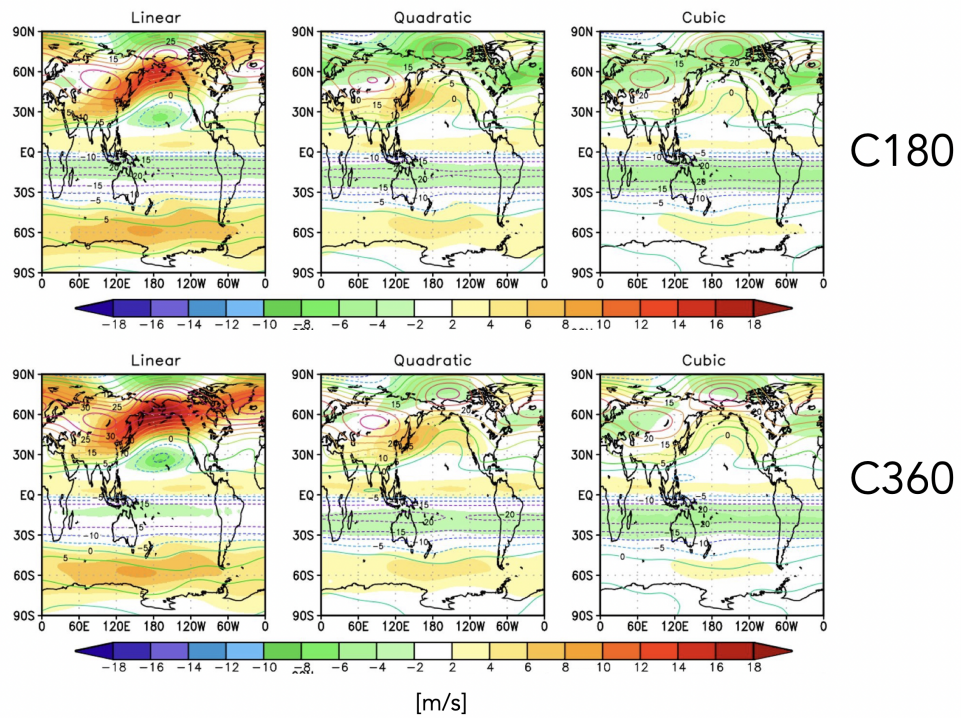


**Figure 14.** Colors shown anomalies in the DJF 1985-2015 climatological mean zonal winds at 30 hPa in the CUBIC (right), QUADRATIC (middle) and LINEAR (left) experiments, relative to MERRA-2. Results for both C180 (top) and C360 (bottom) experiments are shown.

617 quence of the GMAO FV3 remapping scheme but, rather, emerges in tandem with other  
 618 changes that were made in the model. Nonetheless, Figure 8 suggests that improvements  
 619 in transport associated with the GMAO remapping scheme must be carefully weighed  
 620 in the broader context of other model development choices.

621 Interestingly, preliminary analysis suggests that our findings may also translate to  
 622 replay configurations of GEOS (Figure 10), although the effect is muted, relative to free-  
 623 running configurations. As a rigorous evaluation of the stratospheric circulation in re-  
 624 play and DAS configurations is beyond the scope of the current study, future work will  
 625 therefore focus on assessing the extent to which the free-running model biases reported  
 626 here are expressed when the model is run in data assimilation mode. It also bears em-  
 627 phasizing that our findings do have immediate implications for the (free-running) sub-  
 628 seasonal forecast and coupled chemistry climate applications of the GEOS model cur-  
 629 rently in operation.

630 In addition to its implications for GEOS, our results more generally highlight the  
 631 key role played by model numerics in transport (e.g., Rood (1987)). The sensitivities in  
 632 the age-of-air documented herein are also consistent in spirit with the findings in Gupta  
 633 et al. (2020) who showed significant age differences occurring between spectral versus  
 634 finite-volume numerics. Our results, however, suggest that there remain large sensitiv-  
 635 ities even within a given (FV) dynamical core.

636 Looking forward, our findings support and build on the recommendation proposed  
 637 in Gupta et al. (2020) for the construction of dynamical core benchmark tests aimed at  
 638 determining how underlying AGCM numerics impact climatological transport proper-  
 639 ties. In particular, in addition to the age-of-air, the authors propose a range of strato-  
 640 spheric circulation diagnostics that should be evaluated including the zonal mean zonal  
 641 winds, eddy temperature variance and zonal spectra of eddy kinetic energy. Our anal-  
 642 ysis reveals an important role to be played by the climatological zonal mean wind struc-  
 643 ture as it impacts wave convergence over midlatitudes; we therefore also recommend ex-  
 644 plicit consideration of the Eliassen Palm flux convergence and tropical upwelling ( $w^*$ )  
 645 fields as they may be crucial for interpreting age-of-air changes.

646 One somewhat incidental – but practical - result from our analysis is that the statis-  
 647 tics of  $\nabla \cdot \mathbf{F}$  and  $w^*$  are well approximated by ensembles of so-called EMIP integrations.  
 648 As these are substantially easier to run than AMIPs these could provide a “first pass”  
 649 when evaluating new proposed model development changes, without the immediate need  
 650 to integrate AMIP-style experiments. We emphasize, however, that this statement should  
 651 only apply to a first stage in model development as the age-of-air will reflect the time  
 652 integrated impacts of both advection and mixing.

653 Finally, we conclude by noting that, while we have focused on sensitivities within  
 654 the FV remapping algorithm, our results have highlighted important sensitivities to changes  
 655 in radiation and, to a lesser extent, changes in parameterized convection. Though not  
 656 the dominant drivers of the age-of-air changes identified here, the former could poten-  
 657 tially influence the age both directly through changes in thermal structure and indirectly  
 658 by modifying wave propagation and/or generation in the troposphere.



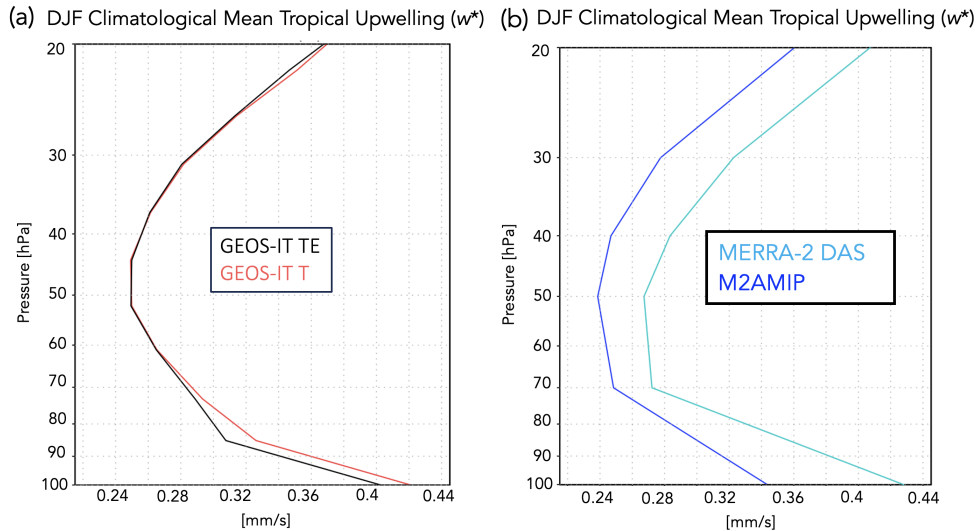


**Figure A1.** The DJF 1985-2015 climatological mean vertical residual mean velocity,  $w^*$ , averaged at each level between the turnaround latitudes compared between two experiments remapping to temperature (T) (red) versus total energy (TE) (black) (a) and between MERRA-2 DAS (cyan) and the M2AMIP ensemble (blue) (b). The underlying model code is consistent with the Version 5.29.4 GEOS-IT model.

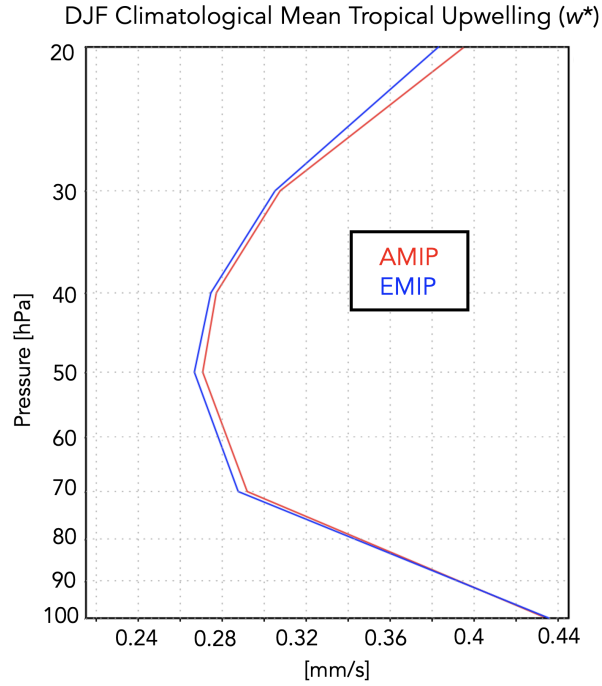
## 659 Appendix A Sensitivities in Calculation of TEM Upwelling

660 There are various aspects of the calculation of the TEM circulation that warrant  
 661 further comment. First, whereas the modeling experiments listed in Table 2 (rows 5-7)  
 662 focus on the sensitivity of Step 5 within the GMAO FV3 core remapping algorithm to  
 663 the choice of interpolation scheme, another difference between the GMAO and GFDL  
 664 FV3 core remapping approaches is the use of TE versus T, respectively. To test the im-  
 665 pact of this difference, we ran a new experiment which is identical to the CUBIC exper-  
 666 iment (Table 2, row 7), except that T is remapped from input layer mean pressure lo-  
 667 cations to standard output layer mean locations directly using cubic interpolation (i.e.,  
 668 no computation of TE or a-posteriori energy conservation applied). Appendix Figure A1a  
 669 shows that this has little impact on the strength of tropical upwelling, suggesting that  
 670 the  $w^*$  differences associated with changes in the remapping algorithm are dominated  
 671 by sensitivities to the choice of interpolation scheme, not the use of TE versus T.

672 Second, the vertical component of the TEM circulation ( $w^*$ ) shows some differences  
 673 in vertical structure between MERRA-2 and the 30-member M2AMIP ensemble (Ap-  
 674 pendix Figure A1b). This difference in vertical structure appears to reflect a difference  
 675 between DAS and free-running configurations of the model, since other DAS configura-  
 676 tions share a similar vertical structure (not shown). Given this difference, we ensure as  
 677 apples-to-apples a comparison of simulated TEM velocities by comparing all AMIP re-  
 678 sults to other AMIP experiments.

## 679 Appendix B Correspondence between EMIP and AMIP Upwelling

680 Appendix Figure B1 shows the close correspondence in DJF climatological mean  
 681  $w^*$ , averaged at each level between the turnaround latitudes, from AMIP and EMIP ex-

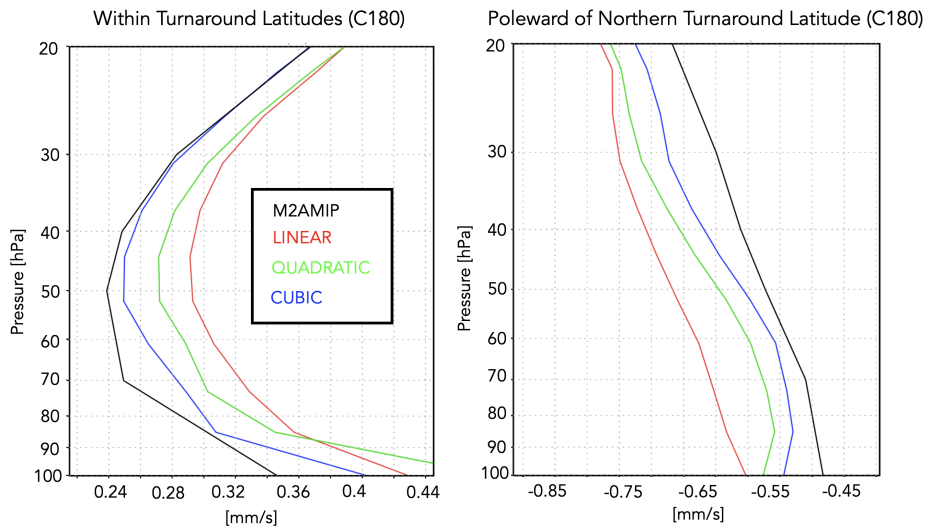


**Figure B1.** The DJF 1985-2015 climatological mean vertical residual mean velocity,  $w^*$ , averaged at each level between the turnaround latitudes for the CTRL experiment (Table 2, row 1). Results based on a 30-year-long AMIP experiment (red line) and a 30-member ensemble of three-month-long EMIP experiments (blue line) are shown.

682 periments using the same model configuration. This good agreement in upwelling is used  
 683 to justify the analysis of the EMIP experiments listed in Table 2 (rows 5-7).

## 684 **Appendix C Changes in Tropical and High Latitude Upwelling**

685 Appendix Figure C1 compares the behavior in residual mean upwelling among the  
 686 LINEAR, QUADRATIC and CUBIC experiments over the latitudes between the (tropi-  
 687 cal) turnaround latitudes (left) and poleward of the northern turnaround latitude (right).  
 688 The ordering among experiments in both regions reflects how increases in downwelling  
 689 at high latitudes are, through mass balance, accompanied by enhanced upwelling in the  
 690 tropics.

DJF Climatological Mean Upwelling ( $w^*$ )

**Figure C1.** Left: The DJF 1985-2015 climatological mean vertical residual mean velocity,  $w^*$ , averaged at each level between the turnaround latitudes for the LINEAR (red line; Table 2, row 5), QUADRATIC (green line; Table 2, row 6) and CUBIC (blue line; Table 2, row 7) experiments. M2AMIP is shown in black. Right: As in left panel, except averaged over latitudes poleward of the northern turnaround latitude. Results in both panels are shown for C180 experiments.

691 **Appendix D Tropopause Pressure**

692 Appendix Figure D1 compares boreal winter tropopause pressure and temperature  
 693 among the LINEAR, QUADRATIC and CUBIC experiments, relative to MERRA-2.

## DJF Climatological Mean Tropopause

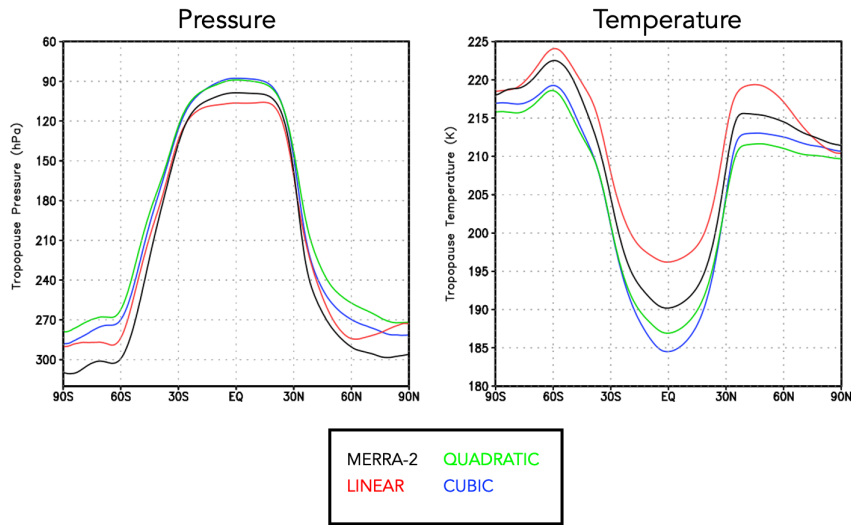


**Figure D1.** The DJF 1985-2015 climatological mean tropopause pressure (left) and temperature (right) in the CUBIC (blue), QUADRATIC (green) and LINEAR (red) experiments. MERRA-2 is shown in black. Results are shown for the C180 experiments.

### 694 Acronyms

- 695 **AMIP** Atmospheric Model Intercomparison Project  
 696 **CH<sub>4</sub>** methane  
 697 **CCMs** chemistry climate models  
 698 **CCMI** Chemistry Climate Modeling Initiative  
 699 **CCMVal** Chemistry Climate Model Validation  
 700 **CO<sub>2</sub>** carbon dioxide  
 701 **CTRL** control  
 702 **CTM** chemistry transport model  
 703 **DAS** Data assimilation  
 704 **DJF** December-January-February  
 705 **EMIP** ensemble AMIP  
 706 **EOS** Earth Observing System  
 707 **EP** Eliassen-Palm  
 708 **FV** finite-volume  
 709 **FP** Forward Processing  
 710 **GEOS** Global Earth Observing System  
 711 **GEOS-R21C** GEOS Retrospective analysis for the 21<sup>st</sup> Century  
 712 **GMI** Global Modeling Initiative  
 713 **HALOE** Halogen Occultation Experiment  
 714 **MERRA-2** Modern-Era Retrospective Analysis for Research and Applications v2  
 715 **MLS** Microwave Limb Sounder  
 716 **N<sub>2</sub>O** nitrous oxide  
 717 **NH** northern hemisphere  
 718 **PPM** piecewise parabolic  
 719 **RRTMG** Rapid Radiative Transfer Model for GCMS

720 **SW** shortwave  
 721 **TE** total energy  
 722 **TEM** Transformed Eulerian Mean  
 723 **UARS** Upper Atmosphere Research Satellite

## 724 Open Research Section

725 All output from the GEOS simulations presented has been reprocessed as GrADS  
 726 control files and binary datasets that are located publicly at <https://gmao.gsfc.nasa.gov/gmaoftp/corbe/StratAge/Data/>. The MERRA-2 data is publicly available at  
 727 <https://disc.gsfc.nasa.gov/datasets?project=MERRA-2>.  
 728

## 729 Acknowledgments

730 C.O. thanks Lawrence Coy and William Putman for their insight which helped in inter-  
 731 preting the results and guiding experimental design. The authors also thank the high-  
 732 performance computing resources provided by NASA’s Advanced Supercomputing (NAS)  
 733 Division and the NASA Center for Climate Simulation (NCCS) as well as NASA’s Mod-  
 734 eling, Analysis and Prediction (MAP) program, which supports the Global Modeling As-  
 735 simulation Office and core chemistry-climate and chemistry-modeling activities.

## 736 References

- 737 Abalos, M., Calvo, N., Benito-Barca, S., Garny, H., Hardiman, S. C., Lin, P., ...  
 738 others (2021). The Brewer–Dobson circulation in CMIP6. *Atmospheric*  
 739 *Chemistry and Physics*, *21*(17), 13571–13591.
- 740 Abalos, M., Orbe, C., Kinnison, D. E., Plummer, D., Oman, L. D., Jöckel, P., ...  
 741 others (2020). Future trends in stratosphere-to-troposphere transport in CCM1  
 742 models. *Atmospheric Chemistry and Physics*, *20*(11), 6883–6901.
- 743 Abalos, M., Randel, W. J., Kinnison, D. E., & Garcia, R. R. (2017). Using the  
 744 artificial tracer e90 to examine present and future UTLS tracer transport in  
 745 WACCM. *Journal of the Atmospheric Sciences*, *74*(10), 3383–3403.
- 746 Andrews, D., Holton, J., & Leovy, C. (1987). Middle Atmosphere Dynam-  
 747 ics. *Academic Press*, *60*, 489. doi: 10.1175/1520-0469(2003)060<0103:  
 748 CEOOAL>2.0.CO;2
- 749 Boering, K. A., Wofsy, S., Daube, B., Schneider, H., Loewenstein, M., Podolske, J.,  
 750 & Conway, T. (1996). Stratospheric mean ages and transport rates from obser-  
 751 vations of carbon dioxide and nitrous oxide. *Science*, *274*(5291), 1340–1343.
- 752 Butchart, N., Cionni, I., Eyring, V., Shepherd, T., Waugh, D., Akiyoshi, H., ...  
 753 others (2010). Chemistry–climate model simulations of twenty-first century  
 754 stratospheric climate and circulation changes. *Journal of Climate*, *23*(20),  
 755 5349–5374.
- 756 Chiodo, G., & Polvani, L. M. (2019). The response of the ozone layer to quadru-  
 757 pled CO<sub>2</sub> concentrations: Implications for climate. *Journal of Climate*, *32*(22),  
 758 7629–7642.
- 759 Chou, M.-D. (1990). Parameterizations for the absorption of solar radiation by O<sub>2</sub>  
 760 and CO<sub>2</sub> with application to climate studies. *Journal of Climate*, *3*(2), 209–  
 761 217.
- 762 Chou, M.-D. (1992). A solar radiation model for use in climate studies. *Journal of*  
 763 *Atmospheric Sciences*, *49*(9), 762–772.
- 764 Chou, M.-D., & Suarez, M. J. (1994). An efficient thermal infrared radiation param-  
 765 eterization for use in general circulation models.
- 766 Collow, A. B. M., Mahanama, S. P., Bosilovich, M. G., Koster, R. D., & Schubert,  
 767 S. D. (2017). *An evaluation of teleconnections over the united states in an*

- 768 *ensemble of AMIP simulations with the MERRA-2 configuration of the GEOS*  
769 *atmospheric model* (Tech. Rep.).
- 770 Davis, N. A., Callaghan, P., Simpson, I. R., & Tilmes, S. (2022). Specified dynamics  
771 scheme impacts on wave-mean flow dynamics, convection, and tracer transport  
772 in CESM2 (WACCM6). *Atmospheric Chemistry and Physics*, *22*(1), 197–214.
- 773 Dietmüller, S., Eichinger, R., Garny, H., Birner, T., Boenisch, H., Pitari, G., ...  
774 others (2018). Quantifying the effect of mixing on the mean age of air in  
775 CCMVal-2 and CCM1-1 models. *Atmospheric Chemistry and Physics*, *18*(9),  
776 6699–6720.
- 777 Eichinger, R., Garny, H., Šácha, P., Danker, J., Dietmüller, S., & Oberländer-Hayn,  
778 S. (2020). Effects of missing gravity waves on stratospheric dynamics: Part 1,  
779 Climatology. *Climate Dynamics*, *54*(5), 3165–3183.
- 780 Eluszkiewicz, J., Hemler, R. S., Mahlman, J. D., Bruhwiler, L., & Takacs, L. L.  
781 (2000). Sensitivity of age-of-air calculations to the choice of advection scheme.  
782 *Journal of the Atmospheric Sciences*, *57*(19), 3185–3201.
- 783 Eyring, V., Lamarque, J.-F., Hess, P., Arfeuille, F., Bowman, K., Chipperfield,  
784 M. P., ... others (2013). Overview of IGAC/SPARC Chemistry-Climate  
785 Model Initiative (CCMI) community simulations in support of upcoming ozone  
786 and climate assessments. *SPARC Newsletter*, *40*(January), 48–66.
- 787 Freitas, S. R., Grell, G. A., Molod, A., Thompson, M. A., Putman, W. M., Santos e  
788 Silva, C. M., & Souza, E. P. (2018). Assessing the Grell-Freitas convection  
789 parameterization in the NASA GEOS modeling system. *Journal of Advances*  
790 *in Modeling Earth Systems*, *10*(6), 1266–1289.
- 791 Gelaro, R., McCarty, W., Suárez, M. J., Todling, R., Molod, A., Takacs, L., ...  
792 others (2017). The modern-era retrospective analysis for research and applica-  
793 tions, version 2 (MERRA-2). *Journal of Climate*, *30*(14), 5419–5454.
- 794 Grell, G. A., & Freitas, S. R. (2014). A scale and aerosol aware stochastic convective  
795 parameterization for weather and air quality modeling. *Atmospheric Chemistry*  
796 *and Physics*, *14*(10), 5233–5250.
- 797 Grooß, J.-U., & Russell III, J. M. (2005). A stratospheric climatology for O<sub>3</sub>, H<sub>2</sub>O,  
798 CH<sub>4</sub>, NO<sub>x</sub>, HCl and HF derived from HALOE measurements. *Atmospheric*  
799 *Chemistry and Physics*, *5*(10), 2797–2807.
- 800 Gupta, A., Gerber, E. P., & Lauritzen, P. H. (2020). Numerical impacts on tracer  
801 transport: A proposed intercomparison test of Atmospheric General Circula-  
802 tion Models. *Quarterly Journal of the Royal Meteorological Society*, *146*(733),  
803 3937–3964.
- 804 Hall, T. M., & Plumb, R. A. (1994). Age as a diagnostic of stratospheric transport.  
805 *Journal of Geophysical Research: Atmospheres*, *99*(D1), 1059–1070.
- 806 Hall, T. M., Waugh, D. W., Boering, K. A., & Plumb, R. A. (1999). Evaluation  
807 of transport in stratospheric models. *Journal of Geophysical Research: Atmo-*  
808 *spheres*, *104*(D15), 18815–18839.
- 809 Hardiman, S. C., Butchart, N., & Calvo, N. (2014). The morphology of the Brewer–  
810 Dobson circulation and its response to climate change in CMIP5 simulations.  
811 *Quarterly Journal of the Royal Meteorological Society*, *140*(683), 1958–1965.
- 812 Haynes, P., McIntyre, M., Shepherd, T., Marks, C., & Shine, K. P. (1991). On the  
813 “downward control” of extratropical diabatic circulations by eddy-induced  
814 mean zonal forces. *Journal of the Atmospheric Sciences*, *48*(4), 651–678.
- 815 Hegglin, M. I., Brunner, D., Peter, T., Hoor, P., Fischer, H., Staehelin, J., ... Weers,  
816 U. (2006). Measurements of NO, NO<sub>y</sub>, N<sub>2</sub>O, and O<sub>3</sub> during SPURT: implica-  
817 tions for transport and chemistry in the lowermost stratosphere. *Atmospheric*  
818 *Chemistry and Physics*, *6*(5), 1331–1350.
- 819 Holton, J. R., Haynes, P. H., McIntyre, M. E., Douglass, A. R., Rood, R. B., & Pfis-  
820 ter, L. (1995). Stratosphere-troposphere exchange. *Reviews of Geophysics*,  
821 *33*(4), 403–439.
- 822 Holzer, M., & Hall, T. M. (2000). Transit-time and tracer-age distributions in geo-

- 823 physical flows. *Journal of the atmospheric sciences*, 57(21), 3539–3558.
- 824 Iacono, M. J., Delamere, J. S., Mlawer, E. J., Shephard, M. W., Clough, S. A., &  
825 Collins, W. D. (2008). Radiative forcing by long-lived greenhouse gases: Cal-  
826 culations with the AER radiative transfer models. *Journal of Geophysical*  
827 *Research: Atmospheres*, 113(D13).
- 828 Ivy, D. J., Solomon, S., Calvo, N., & Thompson, D. W. (2017). Observed connec-  
829 tions of arctic stratospheric ozone extremes to Northern Hemisphere surface  
830 climate. *Environmental Research Letters*, 12(2), 024004.
- 831 Kouatchou, J., Molod, A., Nielsen, J., Auer, B., Putman, W., & Clune, T. (2015).  
832 *GEOS-5 chemistry transport model user’s guide* (Tech. Rep.).
- 833 Legras, B., Pissot, I., Berthet, G., & Lefèvre, F. (2004). Variability of the lagrangian  
834 turbulent diffusivity in the lower stratosphere. *Atmospheric Chemistry and*  
835 *Physics Discussions*, 4(6), 8285–8325.
- 836 Lin, S.-J., Putman, W., & Harris, L. (2017). *The gfdl finite-volume cubed-sphere dy-*  
837 *namical core*. NWS/NCEP/EMC.
- 838 Molod, A., Takacs, L., Suarez, M., & Bacmeister, J. (2015). Development of the  
839 GEOS-5 atmospheric general circulation model: Evolution from MERRA to  
840 MERRA2. *Geoscientific Model Development*, 8(5), 1339–1356.
- 841 Monge-Sanz, B., Chipperfield, M., Simmons, A., & Uppala, S. (2007). Mean age of  
842 air and transport in a CTM: Comparison of different ECMWF analyses. *Geo-*  
843 *physical Research Letters*, 34(4).
- 844 Monge-Sanz, B. M., Bozzo, A., Byrne, N., Chipperfield, M. P., Diamantakis, M.,  
845 Flemming, J., ... others (2022). A stratospheric prognostic ozone for seam-  
846 less Earth system models: performance, impacts and future. *Atmospheric*  
847 *Chemistry and Physics*, 22(7), 4277–4302.
- 848 Morgenstern, O., & Carver, G. D. (2001). Comparison of cross-tropopause transport  
849 and ozone in the upper troposphere and lower stratosphere region. *Journal of*  
850 *Geophysical Research: Atmospheres*, 106(D10), 10205–10221.
- 851 Neu, J., Strahan, S., Braesicke, P., Douglass, A., Huck, P., Oman, L., ... Tegtmeier,  
852 S. (2010). SPARC CCMVal (2010), SPARC Report on the Evaluation of  
853 Chemistry-Climate Models: Chapter 5: Transport. SPARC.
- 854 Neu, J. L., & Plumb, R. A. (1999). Age of air in a “leaky pipe” model of strato-  
855 spheric transport. *Journal of Geophysical Research: Atmospheres*, 104(D16),  
856 19243–19255.
- 857 Oehrlein, J., Chiodo, G., & Polvani, L. M. (2020). The effect of interactive ozone  
858 chemistry on weak and strong stratospheric polar vortex events. *Atmospheric*  
859 *Chemistry and Physics*, 20(17), 10531–10544.
- 860 Orbe, C., Oman, L. D., Strahan, S. E., Waugh, D. W., Pawson, S., Takacs, L. L., &  
861 Molod, A. M. (2017). Large-scale atmospheric transport in GEOS replay simu-  
862 lations. *Journal of Advances in Modeling Earth Systems*, 9(7), 2545–2560.
- 863 Orbe, C., Rind, D., Jonas, J., Nazarenko, L., Faluvegi, G., Murray, L. T., ... oth-  
864 ers (2020). GISS Model E2.2: A climate model optimized for the middle  
865 atmosphere—2. Validation of large-scale transport and evaluation of cli-  
866 mate response. *Journal of Geophysical Research: Atmospheres*, 125(24),  
867 e2020JD033151.
- 868 Orbe, C., Yang, H., Waugh, D. W., Zeng, G., Morgenstern, O., Kinnison, D. E., ...  
869 others (2018). Large-scale tropospheric transport in the Chemistry–Climate  
870 Model Initiative (CCMI) simulations. *Atmospheric Chemistry and Physics*,  
871 18(10), 7217–7235.
- 872 Pan, L. L., Wei, J., Kinnison, D., Garcia, R., Wuebbles, D., & Brasseur, G. P.  
873 (2007). A set of diagnostics for evaluating chemistry-climate models in the ex-  
874 tratropical tropopause region. *Journal of Geophysical Research: Atmospheres*,  
875 112(D9).
- 876 Pawson, S., Stajner, I., Kawa, S. R., Hayashi, H., Tan, W.-W., Nielsen, J. E., ...  
877 Livesey, N. J. (2007). Stratospheric transport using 6-h-averaged winds from

- 878 a data assimilation system. *Journal of Geophysical Research: Atmospheres*,  
879 112(D23).
- 880 Plumb, R. A. (1985). On the three-dimensional propagation of stationary waves.  
881 *Journal of Atmospheric Sciences*, 42(3), 217–229.
- 882 Plumb, R. A. (1996). A “tropical pipe” model of stratospheric transport. *Journal of*  
883 *Geophysical Research: Atmospheres*, 101(D2), 3957–3972.
- 884 Plumb, R. A. (2002). Stratospheric transport. *Journal of the Meteorological Society*  
885 *of Japan. Ser. II*, 80(4B), 793–809.
- 886 Polvani, L. M., Waugh, D. W., Correa, G. J., & Son, S.-W. (2011). Stratospheric  
887 ozone depletion: The main driver of twentieth-century atmospheric circulation  
888 changes in the southern hemisphere. *Journal of Climate*, 24(3), 795–812.
- 889 Prather, M. J., Zhu, X., Tang, Q., Hsu, J., & Neu, J. L. (2011). An atmospheric  
890 chemist in search of the tropopause. *Journal of Geophysical Research: Atmo-*  
891 *spheres*, 116(D4).
- 892 Rood, R. B. (1987). Numerical advection algorithms and their role in atmospheric  
893 transport and chemistry models. *Reviews of geophysics*, 25(1), 71–100.
- 894 Rosenlof, K. H. (1995). Seasonal cycle of the residual mean meridional circulation  
895 in the stratosphere. *Journal of Geophysical Research: Atmospheres*, 100(D3),  
896 5173–5191.
- 897 Son, S.-W., Tandon, N. F., Polvani, L. M., & Waugh, D. W. (2009). Ozone hole and  
898 Southern Hemisphere climate change. *Geophysical Research Letters*, 36(15).
- 899 Strahan, S., Douglass, A., & Newman, P. (2013). The contributions of chemistry  
900 and transport to low arctic ozone in March 2011 derived from aura MLS obser-  
901 vations. *Journal of Geophysical Research: Atmospheres*, 118(3), 1563–1576.
- 902 Thiele, G., & Sarmiento, J. (1990). Tracer dating and ocean ventilation. *Journal of*  
903 *Geophysical Research: Oceans*, 95(C6), 9377–9391.
- 904 Waugh, D., & Hall, T. (2002). Age of stratospheric air: Theory, observations, and  
905 models. *Reviews of Geophysics*, 40(4), 1–1.
- 906 Weaver, C. J., Douglass, A. R., & Rood, R. B. (1993). Thermodynamic balance  
907 of three-dimensional stratospheric winds derived from a data assimilation  
908 procedure. *Journal of Atmospheric Sciences*, 50(17), 2987–2993.